The wedge Topologically Consistent Metamaterial element (wTCM) for the generation of auxetic metamaterials in complex components and its multi-scale numerical calculation with small geometrical and material non-linearities.

Juan Antonio López-Salido[a] and Luis Saucedo-Mora[a]

[a] *E.T.S. de Ingeniería Aeronáutica y del Espacio, Universidad Politécnica de Madrid, Pza. Cardenal Cisneros 3, 28040, Madrid, Spain*

Abstract

Metamaterials are gaining importance in different aspects of engineering because their complex capabilities and light weight ensures a key role in critical elements in different fields. But metamaterials have two main drawbacks; a high computational cost at component level, and a lack of adaptability to complex shapes. This latter point is because traditionally the metamaterials have relied on regular or quasi-regular grids, which is not realistic for more of the engineering needs. In this paper we present the wTCM finite element for the generation of auxetic metamaterials and its multiscale calculation accounting for moderate plasticity, finite strains, and fracture. The proposed element is the opposite the the traditional RVE where a large amount of unit cells are assumed to be inside each RVE. In the case of the wTCM only a portion of the unit cell is represented in the element. With this, we gain versatility and precision with a low computational cost, and the capability to generate the metamaterial from the wTCM mesh directly.

Keywords: Metamaterial, Multiscale model, Plasticity, Fracture, Auxetic

---

1. Introduction

Metamaterials are engineered structures with tailored micro-architectures that enable properties not typically found in natural materials. Unlike conventional materials, whose macroscopic behavior is governed primarily by their chemical composition, metamaterials derive their unique functionalities from their internal geometry and architecture. By carefully designing the disposal of unit cells (setting bar's orientation, size, joints), one can obtain metamaterial structures that exhibit exotic properties which response to mechanical, electromagnetic, thermal, and acoustic fields of research. Several examples of these properties can be found in bibliography, as such as negative refractive index, cloaking effects, band gaps, and programmable deformation patterns, conditioning the final deformed structure to maximize its stiffness [17, 13, 6].

Among the various subclasses of metamaterials with exotic mechanical properties, auxetic metamaterials, which exhibit a negative Poisson's ratio (NPR), have attracted significant interest due to their potential applications. In contrast to most natural materials that contract laterally when stretched, auxetic materials expand in the transverse direction under tension, and contract when compressed, exhibiting a highly unusual but advantageous deformation behavior [12, 24]. This auxetic response arises not from the base material but from the geometrical configuration of the repeating unit cells, which can be designed to deform in non-intuitive ways under applied loads [11].

Auxetic behavior has been observed in a range of architectures, including re-entrant honeycombs, rotating units, chiral lattices, and origami/kirigami-inspired structures [18, 10, 25]. The ability to achieve large, tunable negative Poisson's ratios makes auxetic metamaterials especially attractive for applications requiring enhanced energy absorption, fracture resistance, indentation resistance, and mechanical adaptability [1]. Furthermore, the coupling of auxetic deformation with other mechanical or functional properties has enabled novel applications in biomedical devices, soft robotics, wearable sensors, and acoustic or vibration control systems [19, 3, 23].

Recent advancements in additive manufacturing technologies, particularly high resolution 3D and 4D printing, have significantly expanded the design and manufacturing possibilities for auxetic metamaterials across multiple length scales [26]. At the same time, computational techniques such as topology optimization, finite element modeling, and machine learning-driven design have enabled the systematic exploration of complex design spaces and the discovery of new auxetic topologies with multifunctional behavior [16, 7].

Despite the growing body of work, challenges remain in realizing robust, scalable auxetic structures suitable for real-world conditions. These challenges include understanding failure mechanisms, fatigue behavior under cyclic loading, and achieving tunability and reconfigurability in dynamic environments. One of the key barriers to advancing auxetic metamaterials is the high computational cost associated with simulating their mechanical behavior using solid elements. These simulations, which seem to be necessary to accurately model the complex geometries and deformation mechanisms inherent in auxetic designs, require significant computational resources. This issue becomes particularly pronounced as the size and complexity of cell geometry increase, limiting the feasibility of meso-scale and large-scale simulations with a high level of detail. To fease this challenge, this study investigates the development of a continuous FEM model, which will be equivalent to meso-scale FEM models, carrying out an active update of mechanical properties of the continuos model to reproduce the meso-scale solid model behavior, contributing to the ongoing development on this field.

There are several studies focused on reducing the computational cost of increasing-scale simulations of metamaterial cells. In many cases, the complexity arises from detailed micro-scale specific features, which are related to extremely fine meshes to capture local stress and strain distributions accurately. As a result, the total number of degrees of freedom (DOFs) grows up rapidly, making conventional finite element methods (FEM) prohibitively expensive for meso and large-scale analyses. Recent works have therefore concentrated on developing either multi-scale approaches, where micro-scale effects are "homogenized" or approximated. On the other hand, many efforts are on the development of advanced numerical techniques (e.g., domain decomposition, adaptive mesh refinement, and reduced-order modeling) to accelerate solution times while retaining sufficient accuracy.

For instance, some authors [22] propose a domain-decomposition-based framework in which the computational domain is partitioned into subdomains representing distinct metamaterial cells or repetitive units. By properly matching boundary conditions at interfaces, these subdomains can be solved in parallel, leading to substantial reductions in runtime. In other approaches [9], adaptive mesh refinement (AMR) is used to selectively refine only those regions experiencing high stress gradients while maintaining coarser meshes elsewhere, thereby reducing the total element count.

Moreover, data-driven or surrogate modeling strategies have also gained traction [8]. In these methods, a limited number of high-fidelity simulations or "snapshots" of metamaterial responses are used to train a reduced-order model. This surrogate can then be queried repeatedly—sometimes in near real-time—to approximate the underlying high-dimensional response without needing full-scale FEM computations at every iteration. Such methods are especially beneficial in design optimization loops, where one might need to evaluate hundreds or thousands of candidate geometries.

Overall, these diverse strategies illustrate the continuing effort within the scientific community to balance computational efficiency and accuracy when analyzing meso-scale and macro-scale behavior of complex metamaterial architectures. The following sections provide more contribution to this topic. In this work, a paradigm shift in how meso-scale FEM simulation models are conceived for metamaterial structures is introduced. In fact, the main goal is to simultaneously reduce computational cost and maintain results accuracy for meso scale models, capturing particular behaviours, such as auxetism behaviour in complex metamaterial cells, while keeping an affordable computational cost. To achieve this, the development of a finite element software —entirely implemented in MATLAB— using pentahedral elements is done.

Moreover, the methodology to stabish an equivalence between the detailed solid meso-scale model and continuous model is proposed, developing an updated equivalent Young Modulus methodology for these elements that accounts for the deformation of the internal rods within the metamaterial structure, ensuring that their effect is accurately represented in the continuous model.

The paper is structured as follows. In the methodology we show the capability of the finite element proposed to generate metamaterials in complex geometries and the formulation of the numerical model. Then, in the next section different examples are presented to validate the methodology against detailed numerical models, and experimental tests under different conditions.

2. Methodology

This section introduces an innovative methodology for generating complex auxetic metamaterial structures and multiscale computational models that account for the non-linear effects associated with these structures under several load cases.

2.1. Methodology for auxetic metamaterial generation

The first methodology focuses on designing metamaterial structures with auxetic behaviour based on complex geometries defined using pentahedral elements. Firstly, a geometrical equivalence is established between the auxetic cells and the internal arrangement of bars within the pentahedral elements. A pattern structure is then determined for each cell, formulated from a local reference and composed of a lattice of rods that defines the auxetic behaviour. This lattice is embedded within the volume of each pentahedral element. This internal distribution also enables interpolations to predict the structural configuration of irregular pentahedral elements with local deformations. This approach enables metamaterials with non-periodic structures to be generated, adapted to arbitrary complex geometries. Once the bar distribution within the pentahedral element and the spatial arrangement the bars inside in is known, this configuration can be replicated in space or used as a reference for existing irregular meshes. This enables a metamaterial macrostructure to be constructed by establishing a one-to-one correlation between the domain geometry and the internal bars distribution, thus generating functional geometric configurations adapted to the required design.

Figure 1 shows the internal bar arrangement that defines a metamaterial configuration for a regular structure. It also illustrates the adaptability of this distribution to irregular cells, demonstrating the method's ability to mesh complex geometries, such as the well-known *Rabbit* geometry.

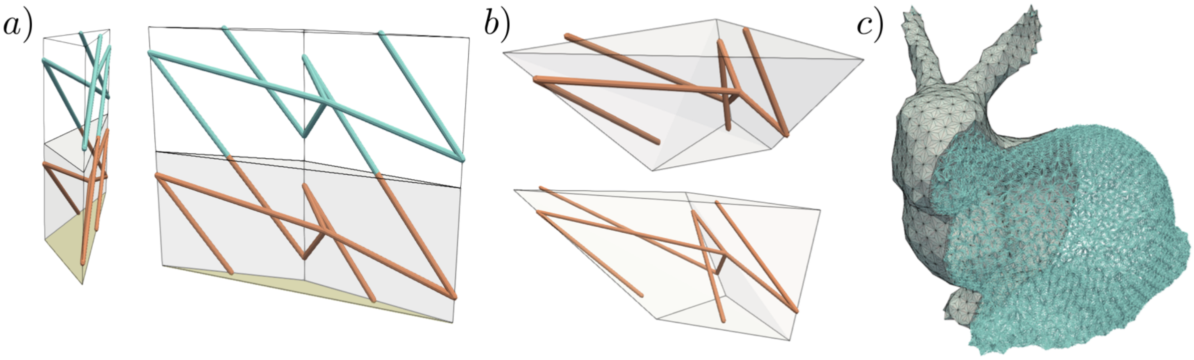

Figure 1: Generation of auxetic metamaterial structures: a) Bars distribution inside a regular pentahedral element. b) Bars distribution inside a non-regular pentahedral element. c) Metamaterial structure generation for complex geometries from the wedge mesh shown.

This methodology enables metamaterial layers to be stacked to create hollow internal geometries (i.e. *Rabbit* mesh in figure), property very useful for aerospace and medical applications.

2.1.1. Local connectivity of the auxetic GAM in the wedge

As mentioned above, this generative methodology is based on a pattern capturing the reference distribution of auxetic metamaterial rods within a pentahedral element. The following example shows how an algorithm can be used to generate the bars distribution corresponding to the geometry of the GAM cell in auxetic configuration within a pentahedral element.

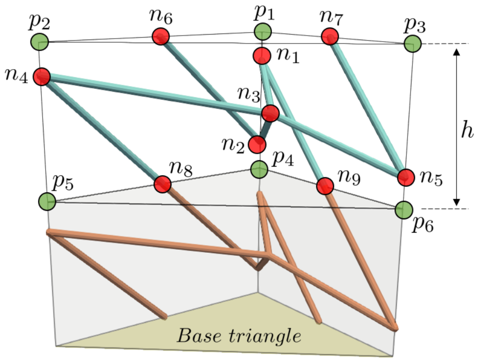

Figure 2: Bars generation inside pentahedral element for GAM auxetic metamaterial cell. Connectiviy between bars and layers.

As can be seen in the above figure, the nodes that define the position of the vertices of the pentahedral elements are denoted as p_i. Using a local reference, the so-called n_i nodes (which determine bars orientation and distribution in penta) are determined for each element. In this case, the image shows that the bars belonging to multiple pentahedral elements have positional continuity in the cut bars, satisfying the conditions $n_6 = n_8$ and $n_7 = n_9$. The generative algorithm for this cell type is analysed in detail below.

Algorithm 1 Wedge based auxetic GAM generation

```
Require: A parametric description of the metamaterial points ($\boldsymbol{n}$) from the pentahedron nodes ($\boldsymbol{p}$).
Ensure: The points of the metamaterial are within the pentahedron.
$n_{1_i} = p_{1_i}\, d + p_{2_i}\, (1-d)$
$n_{2_i} = p_{1_i}\, (1-d) + p_{2_i}\, d$
$n_{3_i} = \frac{p_{1_i}+p_{4_i}}{2}\, (1-c) + \frac{p_{2_i}+p_{3_i}+p_{5_i}+p_{6_i}}{4}\, c$
$n_{4_i} = p_{2_i}\, (1-a) + p_{5_i}\, a$
$n_{5_i} = p_{6_i}\, (1-a) + p_{3_i}\, a$
$n_{6_i} = n_{4_i} - [n_{1_i} + g]$
$n_{7_i} = n_{2_i} - [n_{5_i} + g]$
$n_{8_i} = n_{1_i} - [n_{4_i} - g]$
$n_{9_i} = n_{5_i} - [n_{2_i} - g]$
Where $d \in [0, 0.5)$, $c \in (0, 1)$, $a \in [0, 0.5)$, and $g$ is the height of the pentahedron.
```

2.1.2. Local connectivity of the auxetic cubic in the wedge

Additionally, an algorithm for generating square-based bars distributiosn using the well-known three-dimensional cell for auxetism in metamaterials is presented.

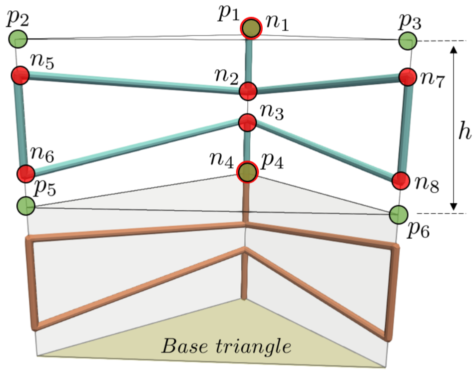

Figure 3: Bars generation inside pentahedral element for cubic auxetic metamaterial cell. Connectiviy between bars and layers.

As in the previous example, the required input is the nodes of the pentahedral elements, p_i, and the output is the nodes that indicate the internal distribution of the bars, n_i. In this case, the bar contained within the edge of the pentahedral element are cut, and in order to keep continuity when this structure is reproduced and stacked in space, it can be seen that the requirement $n_1 = n_4$ must be satisfied. The algorithm developed for generating this type of structure is analysed below.

Algorithm 2 Wedge based auxetic GAM generation

```
Require: A parametric description of the metamaterial points ($\boldsymbol{n}$) from the pentahedron nodes ($\boldsymbol{p}$).
Ensure: The points of the metamaterial are within the pentahedron.
    $n_{1_i} = p_{1_i}$
    $n_{2_i} = p_{1_i}\,d + p_{4_i}\,(1-d)$
    $n_{3_i} = p_{1_i}\,(1-d) + p_{4_i}\,d$
    $n_{4_i} = p_{4_i}$
    $n_{5_i} = p_{2_i}\,c + p_{4_i}\,(1-c)$
    $n_{6_i} = p_{2_i}\,(1-c) + p_{4_i}\,c$
    $n_{7_i} = p_{3_i}\,c + p_{6_i}\,(1-c)$
    $n_{8_i} = p_{3_i}\,(1-c) + p_{6_i}\,c$
Where $d \in (0, 0.5)$, and $c \in [d, 1)$.
```

2.1.3. Application from a Voronoi

Taking as a baseline the methodology previously outlined, the following section presents a methodology for generating heterogeneous macroscale metamaterial structures that employ multiple metamaterial cells and are topologically consistent.

To achieve this, a Voronoi diagram or tessellation is used to generate a two-dimensional polygonal mesh. The centroid of each polygon is extracted. This centroid will be set as the reference point, the dominant point. Specifically, for the proposed example cases, the centroids coincide with the reference points p_1, p_4 (3). From these, the corresponding triangles are generated, which are extruded to create the pentaheral elements.

The metamaterial structure is generated by the use of modules that generate the bars pattern structure within the volumes of the pentas. This results in an irregular and tunable set that offers the possibility of using the cell that best suits the specific requirements of different regions of a single component.

A simple example of the application of this concept is shown in the following image. The upper region shows a regular 2D tessellation composed of hexagons and squares. These evolve into triangles, are extruded to generate penta elements, and the corresponding metamaterial structure is generated. In this case, a congruent transition across the different regions has been modeled, as seen in the figure of the lower region.

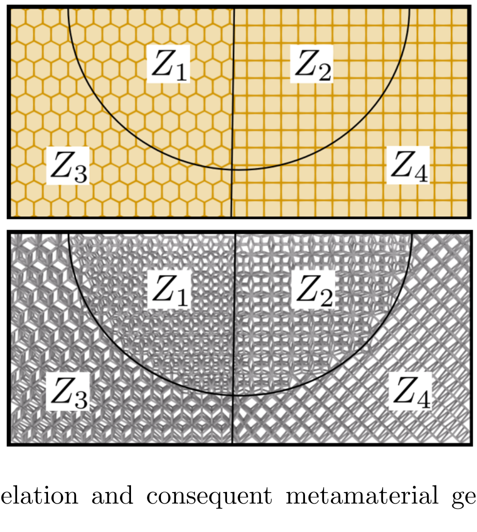

Figure 4: Voronoi regular tesselation and consequent metamaterial generation with several cells and congruent transitions.

As shown in Figure 4, the implementation of this methodology leads to entirely innovative and disruptive designs in the generation of auxetic metamaterial structures. Specifically, the implementation of two regular cells (auxetic GAM and cubic) can be observed, which are modified into different geometric structures across various regions of space. In particular, the region labeled as Z_1 uses a GAM metamaterial cell in an auxetic configuration with a hexagonal base. The Z_2 region uses the same cell but modifying its pattern structure to obtain a square-based cell. The Z_4 region employs the known cubic cell structure with a square base, while the Z_3 egion uses the same cell with a hexagonal base. As evidenced, the potential of the methodology is vast for generating complex, heterogeneous, but topologically consistent structures. The transition from one cell type to another is automatic, and at the interface regions, intersections of bars from the different cell types will form irregular transient lattice structures.

Then, a case is presented where an irregular tessellation is used to push the potential of the methodology to its limits. In Figure (5) a), it can be seen how a regular Voronoi tessellation has been initially generated, which is then disturbed and distorted into irregular geometries. It also shows how the auxetic GAM cell deforms and adapts to these intricate geometries. On the other hand, in Figure b), it is demonstrated how this concept can be extended into three dimensions, generating heterogeneous metamaterial regions and transition structures between them. As shown, the Z_1 region consists of areas formed by a truncated octahedron cell, the Z_2 region is composed of different arrangements of the auxetic GAM cell, and the Z_3 region is made up of various arrangements of the cubic cell.

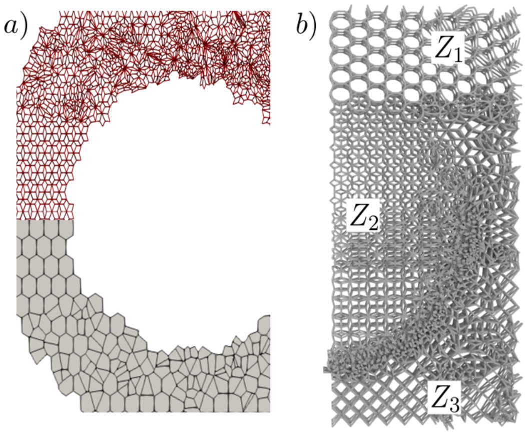

Figure 5: a) Voronoi tesselation and GAM auxetic cell generation for distortioned geometries. b) 3D metamaterial generation from 2D voronoi with different cells and regions. Z_1: truncated octahedron cell. Z_2: GAM auxetic cell. Z_3: cubic auxetic cell.

2.1.4. Application to a .stl file

Finally, an additional example is presented to demonstrate the capabilities acquired for the application of this methodology to complex three-dimensional geometries. In this case, an example is provided for the generation of a metamaterial from a complex geometric model contained in an *.stl* file. Specifically, the geometry of a torus has been chosen, which has a highly complex curvature. On this, several concentrically stacked layers have been developed to create a contour of pentaheral elements with 4 layers. Using the proposed generation methodology, the metamaterial structure associated with the torus has been developed, taking the GAM cell in an auxetic configuration as a reference, and the results are shown below.

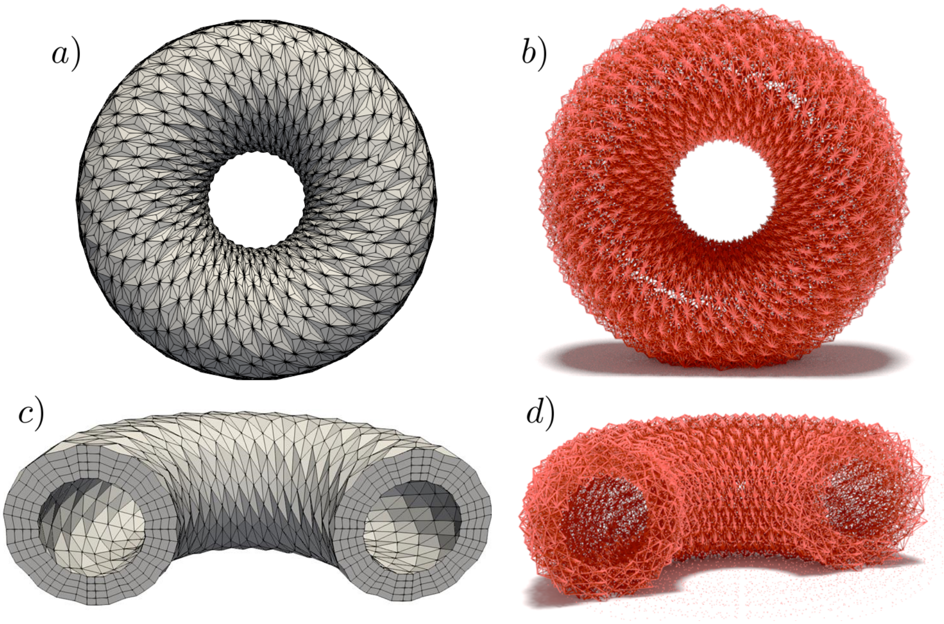

Figure 6: Metamaterial macroscale estructure generation from complex geometry. a) Torus input geometry. b) Torus metamaterial structure. c) Torus pentahedral geometry: layers of pentahedral elements in detail. d) Torus metamaterial structure: metamaterial layers in detail.

In conclusion, the clear capability for generating complex metamaterial structures is evidenced, as seen in the case of the torus, where it is shown how the metamaterial is continuous, congruent, that is, topologically consistent. Furthermore, this approach also enables several research path for the development of advanced computational models that, through the use of pentaheral elements, allow for the modeling of the behavior of complex metamaterial structures, as demonstrated in the following section.

2.2. Simulation methodology for complex metamaterial geometries.

In the same way that a methodology has been carried out focused on the design of irregular metamaterial structures from penta elements, another innovative methodology is proposed now, which enables the simulation of loading cases in metamaterial structures by establishing an equivalence through pentaheral elements.

The outlines of the methodology employed in developing the simulation tool are now presented. First, particular emphasis is placed on the development of features aimed at case configuration, as well as on the formulation of the finite element methodology itself. The finite element model was developed in Matlab, due to that software's ability to perform matrix and vector operations with high agility and optimized resolution.

2.2.1. Methodology inputs

As the developed simulation tool is robust and capable of analyzing a wide range of case types, additional utilities have been created to assist the finite element model in configuring the primary loading scenarios.

Regarding mesh generation, several tools have been developed: these include reading and generating meshes from files containing nodal coordinates and connectivity information, as well as devising pattern-based structures composed of pentahedral elements that can be replicated spatially to form the final finite element mesh. Some examples are shown below:

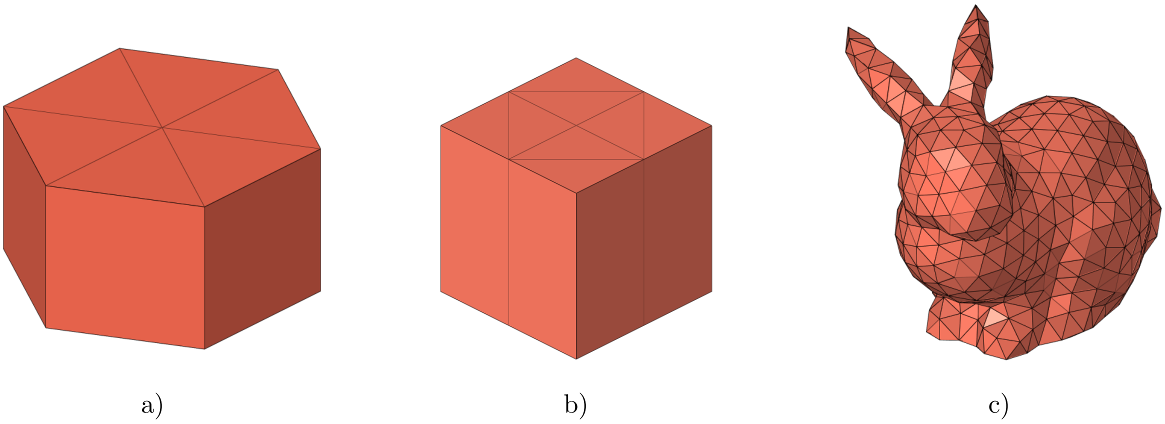
a) b) c)

Figure 7: Pentahedral element meshes. a) Hexahedral pattern mesh. b) Cubic pattern mesh. c) Readable mesh: rabbit.

Additionally, tools have been developed for applying boundary conditions to the model. These tools essentially establish filters to select the nodes on which specific conditions are imposed. Such conditions may range from fully fixed supports at the lower sections to displacement constraints at cross-sections contours, all of which can be tailored to the specific case under analysis.

It is important to note that all cases are solved using displacement control methodology. Considering that certain scenarios may exhibit material nonlinearities (e.g., a non-constant elastic modulus) and geometric nonlinearities (e.g., large displacements), the application of displacements step by step (or incremental displacements) allows the equilibrium path of the structure to be tracked even beyond the peak load, thereby accurately capturing nonlinear responses or stiffness degradation. Several utilities have been developed to support different displacement-imposition schemes: uniform displacements on specific mesh boundaries, custom displacements on particular nodes, or advanced configurations for indentation cases, depending on the requirements of each scenario.

On the other hand, an auxiliary utility is developed to generate more advanced input required data. To establish equivalence between the continuous model of pentahedral elements and the discrete metamaterial bar model, it is necessary to determine which bars lie within each pentahedral element.

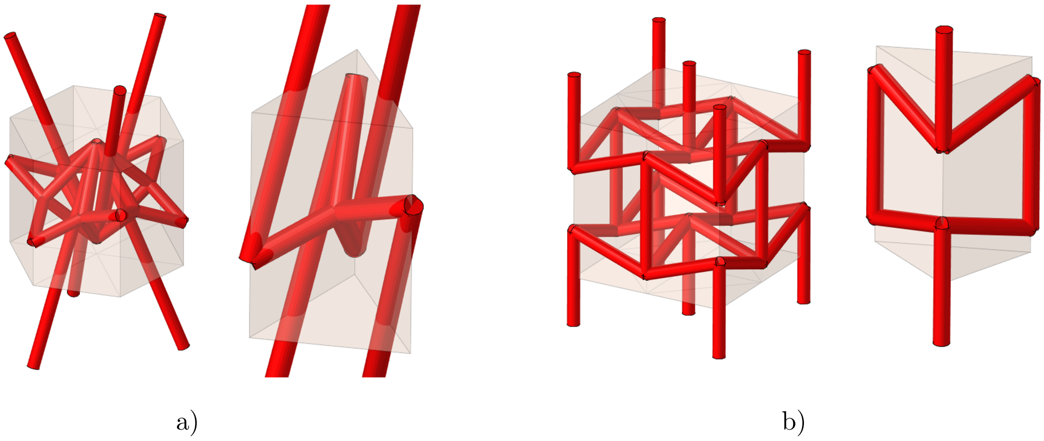
a) b)

Figure 8: Bars inside pentas. a) GAM auxetic cell. b) Cubic cell.

To this end, an external tool is created and its main function will be associating all the model bars with each pentahedral element, as well as to define their orientation inside the element.

As can be seen in the Figure 8, the metamaterial's bars are not fully contained within each pentahedral element. To address this, the location of each bar's centroid is evaluated to determine which pentahedral element it belongs to. In addition, some bars have multiple associations because they lie on faces, edges, or vertices of the element. It is assumed that the effects of such shared bars will be distributed evenly among the pentahedral elements containing them. Consequently, a distribution factor (DF) is introduced, which is defined as the inverse of the number of pentahedral elements that share a bar, $DF = 1/N_{shared\ elm.}$.

Finally, the type of analysis to be performed is configured. As previously mentioned, the ultimate aim of this simulation tool is to develop an equivalent model that reproduces the nonlinear behavior of meso-scale auxetic models with highly complex metamaterial structures (composed of a large number of bars). However, the final state of the simulation tool has been achieved incrementally. First of all, simpler models that have been continually subjected to correlation procedures have been developed, so several types of solutions have been sequentially included in the tool. The cases to be solved can then be divided into two categories: those where Young's modulus remains constant (corresponding to a static linear-elastic case solvable by commercial software), and advanced scenarios where material nonlinearity is introduced through the use of an equivalent Young's modulus that capture the deformation state of the bars using a specific procedure for each pentahedral element.

2.2.2. FEM simulation algorithm.

The development of the simulation algorithm was conceived in several stages. First, a basic implementation was conducted for a model based on pentahedral elements. This model incorporates the classical shape functions for this type of element, as commonly employed in commercial FEM softwares [15, 14]. There exist multiple ways of defining isoparametric coordinates reference systems, but all of them are valid if the element connectivity matrix is designed to be consistent with the respective shape functions.

Applying the conventional finite element methodology [4], a local stiffness matrix is generated for each pentahedral element based on the material's elastic constants tensor, and these local matrices are then assembled to obtain the global stiffness matrix. Considering both the restricted DoFs and imposed displacement DoFs (both treated as inputs derived from the case configuration), the calculation of the equivalent force vector is performed. Once this vector is obtained, the unknown displacements at the free degrees of freedom are determined, leading to the final global displacement vector and the global force vector. This methodology, used to solve linear static cases with small displacements, can be employed to progressively calculate incremental displacement values —from the initial state through to the final desired displacement— in order to capture the structure's deformation path under a gradually applied load. At this point in the development, this concept is based on the resolution of N_{steps} static cases.

The development of this methodology has been correlated by comparison with analogous models implemented in the commercial software MSC Nastran. Specifically, the model in that software was given a mesh identical to the one used in Matlab (including same node IDs and element IDs). A linear elastic material model with the same material parameters was included too, as well as analogous boundary conditions, matching displacement values and its directions (applied to the same degrees of freedom). Once the analysis was carried out, nodal displacements, nodal forces, stress and strains values in global coordinates, von Mises stresses, and strain energies were compared, leading to deviations of less than 0.01%. This outcome validates the developed FEM tool and establishes it as the baseline for extending the analogy to lattice-based metamaterial models.

Once the finite element model has been developed, the next step is to establish the equivalence between the continuous model and the respective metamaterial structure. To do this, an equivalent elastic modulus E_eq is calculated for each element. This modulus is continually updated and depends directly on the deformation state of the bars within each element.

Therefore, for a specific imposed displacement step, the process described above is carried out, obtaining nodal displacements, nodal forces, stresses, strains, and strain energies.

Subsequently, a sweep is performed for all elements in the structure, extracting each element's associated strain tensor. Assuming that most of the bar deformation arises from axial loading, the strain tensor is projected onto the axial direction of each bar contained in the pentahedral element. This projection yields the axial strain of each bar within the element and, consequently, its axial displacement:

$$\varepsilon_{bar} = \mathbf{n_{bar}} \cdot \boldsymbol{\varepsilon_{element}} \cdot \mathbf{n_{bar}} \tag{1}$$

$$u_{bar} = |\varepsilon_{bar} \cdot L_{bar}| \tag{2}$$

This assumption holds for the majority of metamaterial structures that work under axial loads, including nonlinear scenarios such as impacts or indentations, and it is therefore considered as valid for a wide range of applications.

Once the axial displacement is obtained, correlation curves, which retain all the nonlinear effects of bars are analyzed. These curves can be calibrated for each type of cell and their values and tendencies can involve various effects, such as the equivalent constraints at each bar's endpoints for each structural typology, as well as the bar's stress state (tension or compression) inside the specific cell under a macroscopic given load condition. Once these curves are determined, an interpolation is performed to obtain the the effect of this conditions acting on the bar. Finally, the element's strain energy is computed as the sum of the strain energy of all bars contained within the pentahedral element. The strain energy of each bar is multiplied by its corresponding distribution factor DF, ensuring the energy es equally distributed among all elements that share each bar.

$$U_{bars\ element} = \sum_{i=1}^{n_{bars}} DF_i \cdot u_{bar_i} \cdot \frac{dW_e}{du_{bar_i}} \tag{3}$$

On the other hand, since a linear elastic material model was employed, the elastic material tensor can be expressed as follows:

$$\mathbb{C}(E, \nu) = E \cdot \mathbb{C}_{\text{without}}(\nu) \tag{4}$$

Then, the strain energy of the pentahedral element can be computed as:

$$\boldsymbol{\sigma_{elem}} = \mathbb{C}(E, \nu) \cdot \boldsymbol{\varepsilon_{elem}} = E \cdot \mathbb{C}(\nu) \cdot \boldsymbol{\varepsilon_{elem}} \tag{5}$$

$$U_{penta,elem} = \frac{1}{2}\boldsymbol{\sigma_{elem}} \cdot \boldsymbol{\varepsilon_{elem}} \cdot V_{elem} = \frac{1}{2}E \cdot \mathbb{C}(\nu) \cdot \boldsymbol{\varepsilon_{elem}} \cdot \boldsymbol{\varepsilon_{elem}} \cdot V_{elem} \tag{6}$$

These two ways to determine strain energy for the element must result in the same strain energy value, so an equivalent Young Modulus can be calculated as:

$$E_{updated,element} = \frac{U_{penta,element}}{U_{bars,element}} \tag{7}$$

This calculation is going to be done iteratively for each load step untill achieving convergence (comparing forces deviation between iterations). This will result in a material nonlinearity, as every element will have its specific equivalent Young Modulus, which will be evolving for each imposed displacement step. The workflow is shown in Algorithm 3 present in the Annex.

As anticipated, the potential of this methodology is substantial, since it offers a significant reduction in computational cost relative to lattice bar models. The decrease in the number of degrees of freedom spans multiple orders of magnitude, and during the validation phase, the difference in computational cost between the lattice bar models and the equivalent continuous models will be demonstrated. In the following sections, the proposed methodology will be validated by employing various validation strategies to confirm its robustness and its application.

3. Validation.

After developing the complete methodology for establishing the equivalence between the continuous medium model and the meso-scale model, a validation strategy will be introduced to assess its effectiveness across various scenarios.

This validation strategy involves the development of meso-scale finite element models conducting nonlinear FEM simulations for each case study.

As explained, the study focuses on auxetic-type cells, so the validation cases will be developed through the design of meso-scale structures composed of different cells of this type. The main purpose of using this type of cell lies in the fact that their morphology is ideal to stablish an equivalence in pentaheral elements for the vast majority of cases. Moreover, this methodology allows for a straightforward and approachable study to quantify the auxetic behavior in metamaterial structures developed with this type of cell.

One of the proposed cells is the GAM (General Auxetic Metamaterial) cell [5, 21]. This cell has the particularity of developing different behaviors depending on the connectivity of the different metamaterial layers, thus achieving either an auxetic or non-auxetic global behavior. Additionally, another type of auxetic cell is used. This type of cell has been widely used in its 2D version for the identification and characterization of auxetism, and its 3D version is used for the analysis in this work [20].

GAM Cell								**Cubic Cell**
$\mathbf{v_1}$	$\mathbf{v_2}$	$\mathbf{Step_x}$	$\mathbf{Step_y}$	$\mathbf{H_{star}}$	$\mathbf{D_{star}}$	$\mathbf{H_{prism}}$	**Dimensions [mm]**	**Dimensions [mm]**
-0.4	0.2	1	1	0.25	0.3	1.6	2x2x1.6	$\sqrt{2}$x2x2$\sqrt{2}$

Table 1: Auxetic and non auxetic cell structure parameters.

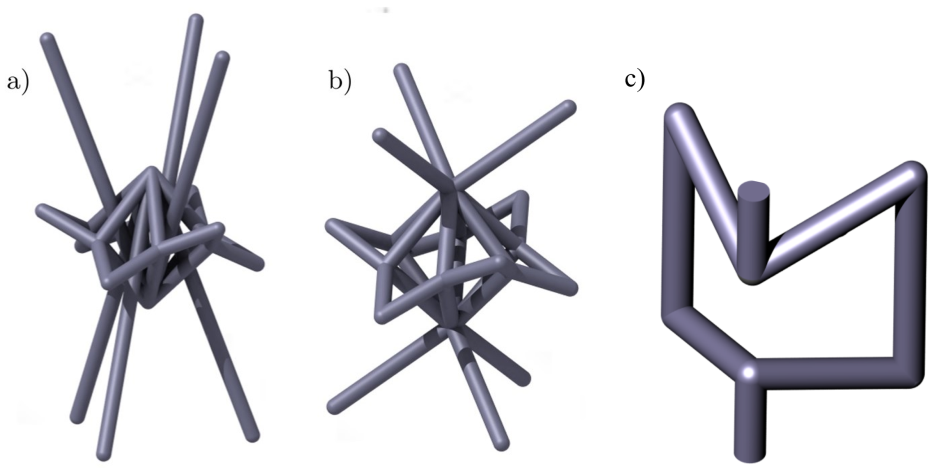

Figure 9: Metamaterial cells. a) GAM Auxetic cell. b) GAM Non Auxetic cell c) Cubic cell.

The cell parameters set out above will be the ones used for all cases unless explicitly stated otherwise. From these parameterised cells, the meso-scale models are constructed by means of solid elements that model the lattice bar structure. These structures will be constructed using pentaheral elements that faithfully reproduce the geometry of each specific lattice. To ensure accurate representation of bar thickness effects, the meshing will be refined such that at least three elements span the thickness dimension. This approach represents a high-fidelity simulation technique, typically employed for comprehensive analysis of metamaterial cell behavior, albeit with a significantly higher computational cost.

Materials							
Cases	**Material model**	**E [MPa]**	$\boldsymbol{\nu}$	**G [MPa]**	$\boldsymbol{\sigma_y}$ **[MPa]**	$\mathbf{E_t}$ **[MPa]**	**B [MPa]**
Meso-Scale MAT1	linear elastic	210000	0.3	–	–	–	–
Meso-Scale MAT2	isotropic hardening	–	–	79300	360	21000	$1.6 \cdot 10^6$
Penta GAM Aux.	Y.M. Updates	210000	-0.12	–	–	–	–
Penta GAM Non Aux.	Y.M. Updates	210000	0.3	–	–	–	–
Penta Cubic Aux.	Y.M. Updates	210000	-0.2	–	–	–	–
Penta 3D Exp. Aux.	Y.M. Updates	210000	-0.2	–	–	–	–
Penta 2D Exp. Aux.	Y.M. Updates	210000	-0.2	–	–	–	–

Table 2: Material properties used in the analysis

Depending on the case, simplier or more complex materieals models will be used (from elastic material models to elastoplastic models with isotropic hardening). The units for the bar lattice models will always be the same: length $[mm]$, stress $[MPa]$, force $[N]$, density $[kg/mm^3]$, Young's modulus $[MPa]$.

Depending on the level of correlation, models without contact between bars and models with contact between them will be developed, and their influence on the final validation obtained will be studied.

The ultimate goal of the validation strategies will be to demonstrate the robustness of the methodology in a wide variety of different cases and situations. In each case, specific subcases will be presented, showing strong and weak possible points of the methodology. To summarize the validation process, a table with all the main information of each case is developed now.

3.1. Case one: increase domain progressively.

In this case, the objective is to demonstrate that the calibration of the curves for the different bars that make up the unit cell is robust and can be extended to different

Meso-Scale Validation Cases					
Case ID	**Cell Type**	**Domain**	**Material Model**	$\mathbf{R_{bars}}$	**Observations**
1 a)	GAM Aux. Cell	1x1x2	linear elastic	0.07	Axial compression. No bar's contact
1 b)	GAM Aux. Cell	2x2x2	linear elastic	0.07	Axial compression. No bar's contact.
1 c)	GAM Aux. Cell	6x6x7	linear elastic	0.07	Axial compression. No bar's contact.
2 a)	GAM Aux. Cell	6x6x7	isotropic hardening	0.09	Axial compression. Reduced Height
2 b)	GAM Aux. Cell	6x6x7	isotropic hardening	0.07	Axial compression. Reduced Height
2 c)	GAM Aux. Cell	6x6x7	isotropic hardening	0.05	Axial compression. Reduced Height
2 d)	GAM Aux. Cell	6x6x7	isotropic hardening	0.03	Axial compression. Reduced Height
3 a)	GAM Aux. Cell	6x6x7	isotropic hardening	0.07	Axial free compression.
3 b)	GAM Aux. Cell	6x6x7	isotropic hardening	0.07	Axial free tension.
3 c)	GAM Aux. Cell	6x6x7	isotropic hardening	0.07	Axial constrained compression.
3 d)	GAM Aux. Cell	6x6x7	isotropic hardening	0.07	Axial constrained tension.
3 e)	GAM Non Aux. Cell	6x6x7	isotropic hardening	0.07	Axial free compression.
3 f)	GAM Non Aux. Cell	6x6x7	isotropic hardening	0.07	Axial free tension.
3 g)	GAM Non Aux. Cell	6x6x7	isotropic hardening	0.07	Axial constrained compression.
3 h)	GAM Non Aux. Cell	6x6x7	isotropic hardening	0.07	Axial constrained tension.
4 a)	GAM Aux. Cell	10x10x7	isotropic hardening	0.07	Indentation.
5 a)	Cubic Aux. Cell	3x3x7	isotropic hardening	0.11	Axial free compression.
5 b)	Cubic Aux. Cell	3x3x7	isotropic hardening	0.11	Axial free tension.
5 c)	Cubic Aux. Cell	3x3x7	isotropic hardening	0.11	Axial constrained compression.
5 d)	Cubic Aux. Cell	3x3x7	isotropic hardening	0.11	Axial constrained tension.
6 a)	Exp. Aux. 3D Cell	1x1x1	tabulated material	1.6	Experimental 3D cell compression.
6 b)	Exp. Aux. 2D Cell	1x1x1	tabulated material	1.6	Experimental 2D cell tension.
7 a)	Sphere GAM Aux.	Complex	isotropic hardening	0.07	Simulation of complex geometry.

Table 3: Parameters of the validation cases.

metamaterial volumes for a given unit cell. For this case, GAM Auxetic cell will be used.

To this end, three subcases are proposed, in which the domain will be progressively increased. The domain sizes in the respective subcases are: 1x1x2 cells, 2x2x2 cells, and 6x6x7 cells. In the detailed models, a linear elastic material model will be employed, with material parameters provided in Table 2.

Additionally, no contact between the bars is considered, and a progressive compression will be applied, with a magnitude of -0.6 mm for the smallest-volume subcase and -1 mm for the other subcases.

For the equivalent pentahedral model, the material parameters specified in Table 2 for this type of cell will also be used.

As can be observed, the Poisson's ratio used is an equivalent value that models the auxetic behavior of the cell for this case. Therefore, the three subcases are analyzed for both the lattice models and the reduced model. The results for the different subcases are presented below, grouped by graphs.

As can be observed in Figures (10) and (11), the stiffness degradation in the force – displacement curve is due to the buckling of the vertical connectivity bars. This phenomena accurately captured by the continuum model. The analysis now proceeds with the subcase involving larger dimensions:

As shown, the correlation between the detailed model and the equivalent continuum model is also accurate in this subcase. The calibration curves used across all cases are those shown in Figure (12), which supports the conclusion that the proposed methodology is robust for scenarios in which the domain varies but the unit cell remains the same. Finally, a comparative analysis of the stress field is conducted for the last subcase:

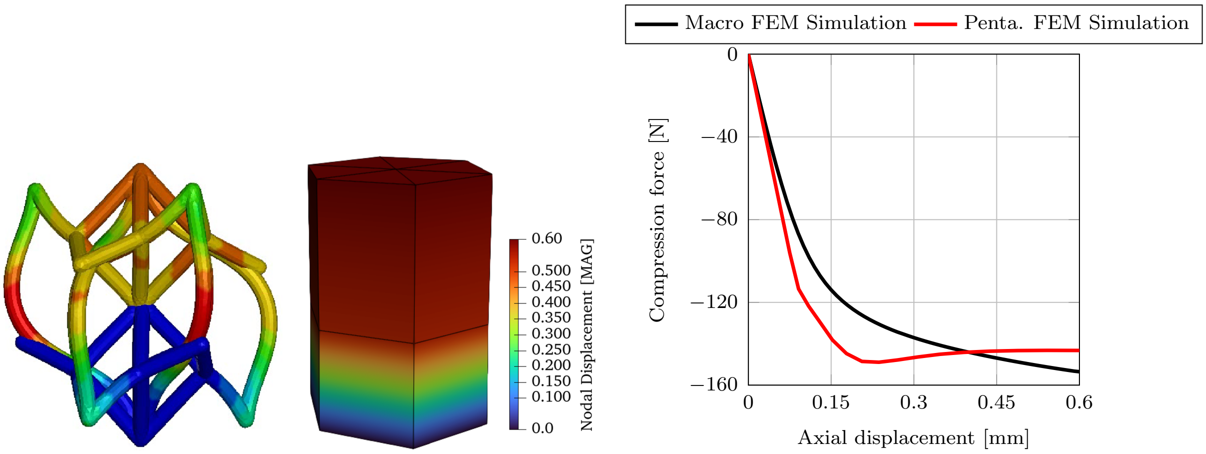

a.1)

a.2)

Figure 10: Subcase 1 a) results: a.1) Displacement field for -0.6mm compression load. a.2) Force-displacement curve for axial compression subcase a).

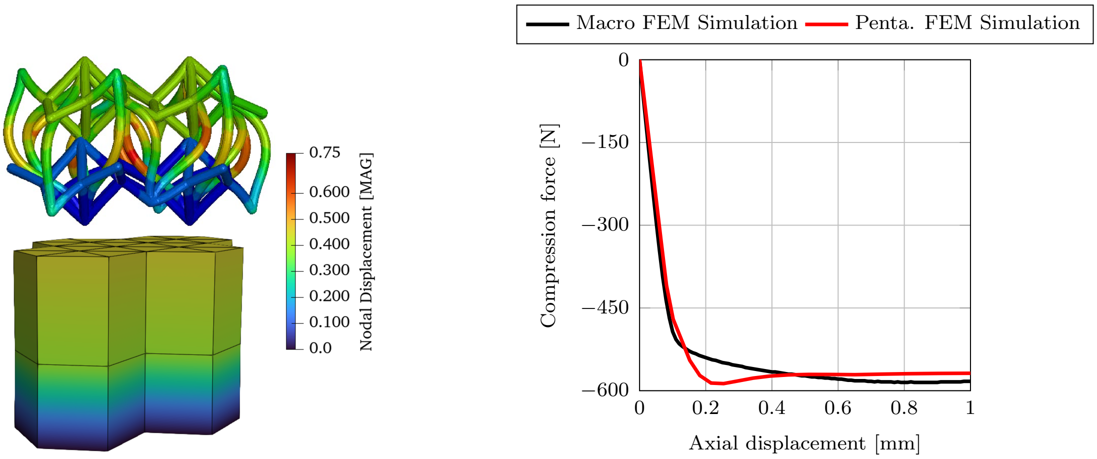

b.1)

b.2)

Figure 11: Subcase 1 b) results: b.1) displacement field for both cases. b.2) Force-displacement curve for axial compression subcase b).

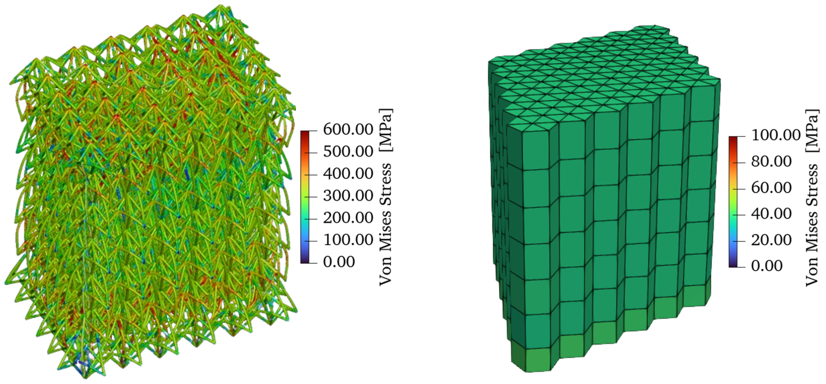

Figure 13: Macro FEM tetahedral free subcases.

In view of the Figure (13), the stress field captured in the pentahedral elements model does not match the one found inn bars model. This is expected, since the continuum

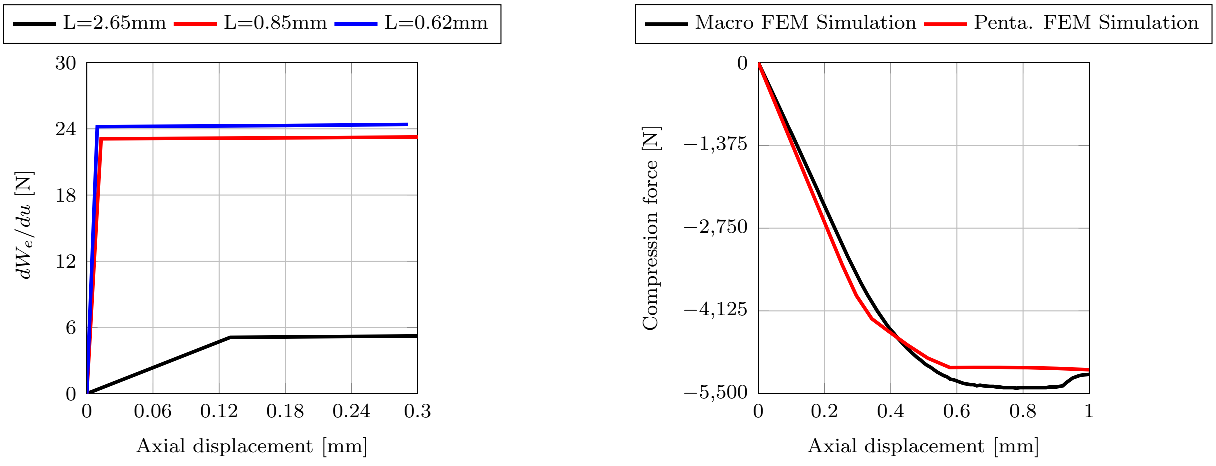

c.1) c.2)

Figure 12: Subcase 1 c) results: c.1) calibration curves for all subcases in case 1. c.2) Force-displacement curve for axial compression subcase c)

model represents an averaged stress state of the element, as a consequence of the stress states of the bars contained within it.

3.2. Case two: change in bar's radii.

Once the generalization of the methodology for incrementally scaled volumes of the same unit cell has been demonstrated, the study proceeds to analyze how changes in the cell's parameters affect the corresponding correlation.

To this end, a series of subcases is developed in which the radius of the lattice bars within the cell is varied, while all other parameters remain constant. The direct influence of the bar radius on the correlation curves is analyzed. This parameter is critical and requires specific calibration of the curves for each proposed subcase.

Specifically, the proposed radii for the different subcases will be analyzed based on a slenderness parameter. This slenderness will be calculated as the quotient of the length of the characteristic longest bar and the radius of gyration (ρ) of the circular section. It is important to remember that ρ takes the value of $R_i/2$ for circular sections. Taking this into account, the slenderness parameter is as $\lambda_i^* = 2 \cdot L_{bar}/R_i$. Where R_i is the cross-section radius of the bars and L_{bar} takes the value of 2.51 mm in all cases (as they are geometrically identical).

$\lambda_\mathbf{1}^*$	$\lambda_\mathbf{2}^*$	$\lambda_\mathbf{3}^*$	$\lambda_\mathbf{4}^*$
55.73	71.66	100.32	167.20

Table 4: Slenderness values for different cases.

Furthermore, in the detailed model subcases, an elastoplastic material model with isotropic hardening has been used, and contact interactions between the bars have been included, as shown in Table 2.

The following section presents the calibration curves specific to each subcase, along with the axial compression force-displacement resultant curves, associated with each subcase.

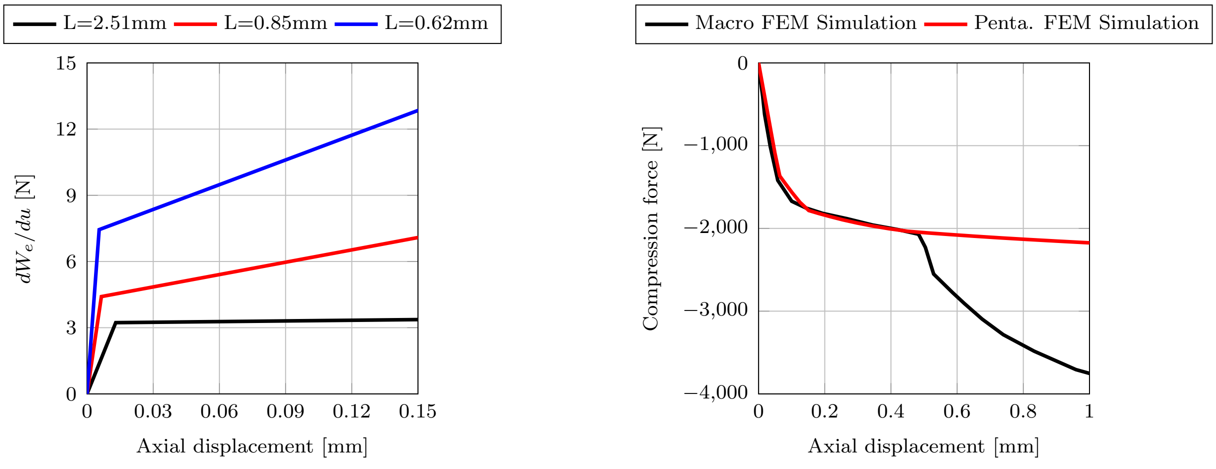

a.1) a.2)

Figure 14: Subcase 2 a) results: a.1) Correlation curves for λ_1^* slenderness. a.2) axial force-displacement curve for a) subcase.

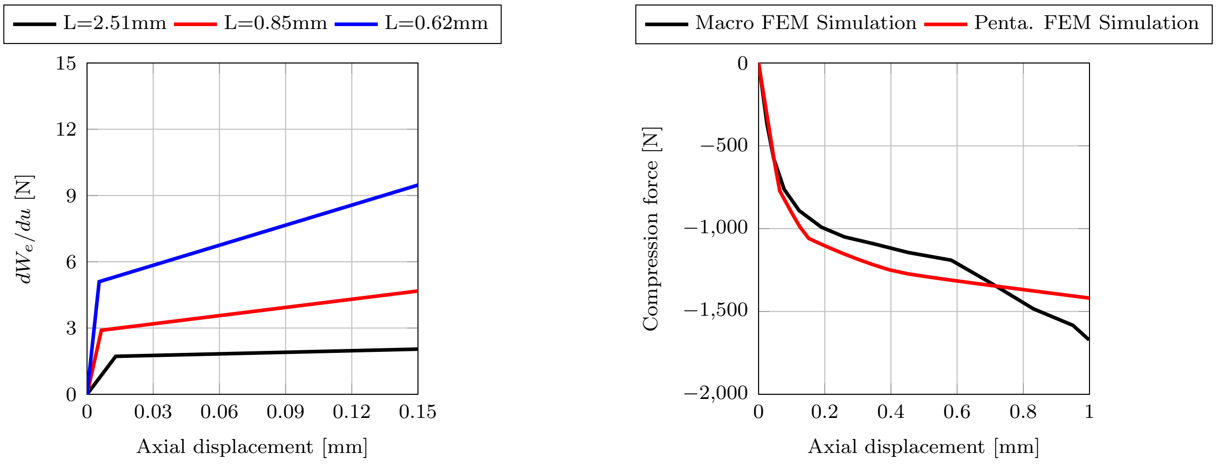

b.1) b.2)

Figure 15: Subcase 2 b) results: b.1) Correlation curves for λ_2^* slenderness. b.2) axial force-displacement curve for b) subcase.

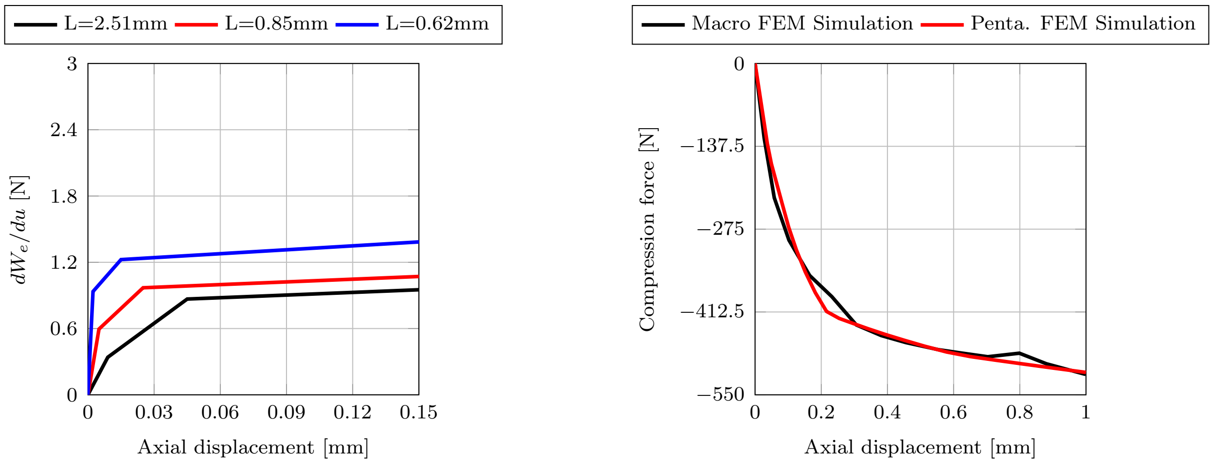

c.1) c.2)

Figure 16: Subcase 2 c) results: c.1) Correlation curves for λ_3^* slenderness. c.2) axial force-displacement curve for c) subcase.

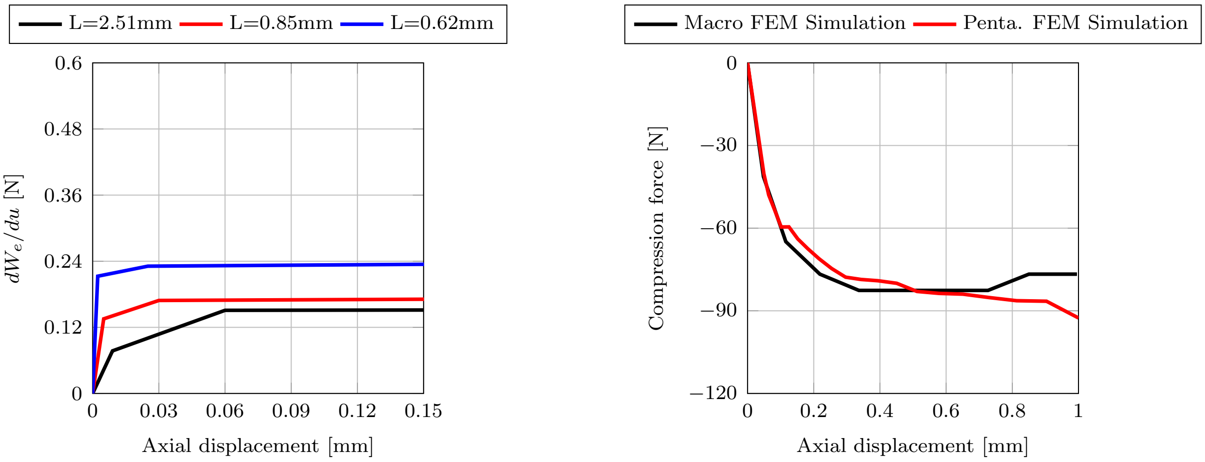

d.1) d.2)

Figure 17: Subcase 2 d) results: d.1) Correlation curves for λ_4^* slenderness. d.2) axial force-displacement curve for d) subcase.

In view of the results, the following conclusions can be drawn:

- The calibration is consistent. The calibration curves progressively decrease as the bar radius decreases.
- The axial force–displacement curves recorded for both models in each subcase show a very high degree of correlation.
- In the axial force-displacement curves where the slenderness is smaller, it is clearly observed how the bars come into contact with each other quickly, resulting in additional stiffness provided by the interference between the bars. As the slenderness increases, the interference decreases, eventually disappearing in the subcases with the highest slenderness.

3.3. Case three: auxetism effect for different cells configuraton.

The following case analyzes the effect of auxetism on GAM-type cells in both auxetic and non-auxetic configurations. To this end, a structure of 6×6×7 GAM cell lattice is carried out, and several subcases are developed. In this case, an elastoplastic material model with isotropic hardening is used, and the effect of bar interference is also considered. Unlike the previous case, the height between layers is increased to its nominal value, while the other bars remain the same length. Therefore, under same cell parameters, material model, boundary conditions, and contact model, the previous correlation for slenderness corresponding to a bar radius of $R = 0.07$ mm is preserved, and the calibration curve of the longest bar is proportionally adjusted, allowing the calibration curves to be obtained quickly for the GAM auxetic cell configuration. In all cases, compression and tension loads will be analyzed based on imposed displacements with a magnitude of 1.5 mm.

Initially, four cases are analyzed for the GAM cell in the auxetic configuration. Subcases a) and b) correspond to free axial compression and tension, respectively. Subcases c) and d) correspond to axial compression and tension where cross movements are restricted, thereby quantifying the auxetic effect of the structure.

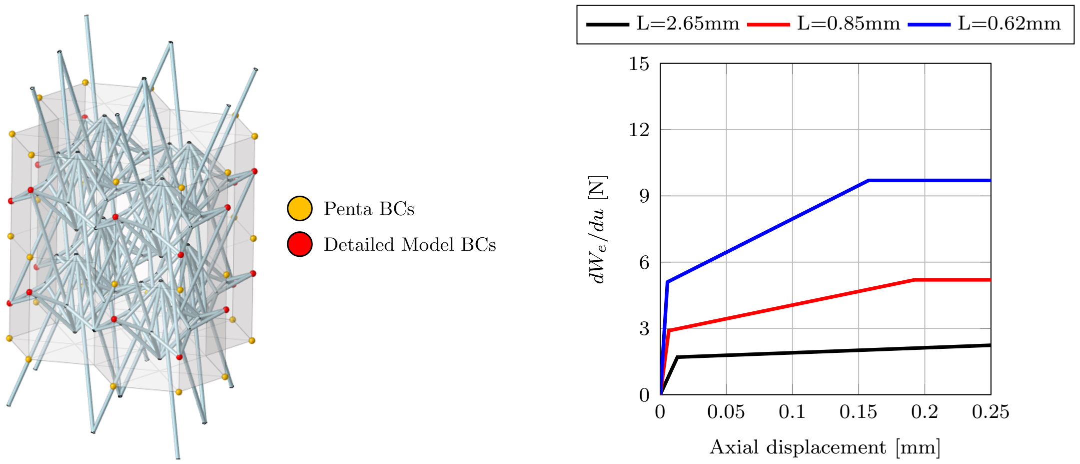

a)

b)

Figure 18: a) Contour boundary condition for both deailed and penta model for GAM auxetic structure. b) Elastic energy correlation curves for GAM auxetic cell, considering $R = 0.07$ mm, nominal cell height, elastic plastic material and contact between bars.

For this cell configuration, the boundary condition imposed on the lateral contour of the pentahedral elements is excessively restrictive and does not adequately reproduce the constrained movement of the vertices at the vertices of the lattice structure. Therefore, a correction factor α is introduced in the strain tensor while calculating strain energy, such that the strain tensor in the contour elements takes the following form:

$$\boldsymbol{\varepsilon}_{\text{contour}} = \alpha\,\boldsymbol{\varepsilon} = \alpha \begin{pmatrix} \varepsilon_{xx} & \varepsilon_{xy} & \varepsilon_{xz} \\ \varepsilon_{xy} & \varepsilon_{yy} & \varepsilon_{yz} \\ \varepsilon_{xz} & \varepsilon_{yz} & \varepsilon_{zz} \end{pmatrix} \tag{8}$$

This correction factor helps to accurately reproduce the equivalent boundary condition in the detailed model. Based on this criterion, a factor of $\alpha = 2.5$ is required to precisely capture the effect of the transverse constraints in GAM auxetic cell. With these assumptions, the following figures presents the axial and transverse forces for each case of the GAM cell in the auxetic configuration, comparing the results obtained from the detailed model with those from the pentahedral element model.

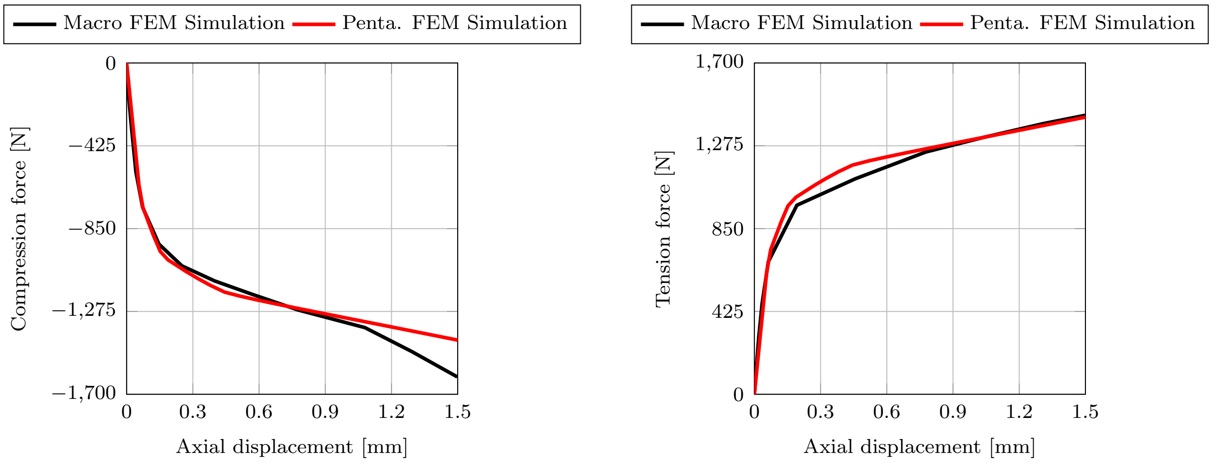

a)

b)

Figure 19: Results for 3 a) and 3 b) subcases: a) axial force-displacement curve for free compression case. b) axial force-displacement curve for free tension subcase.

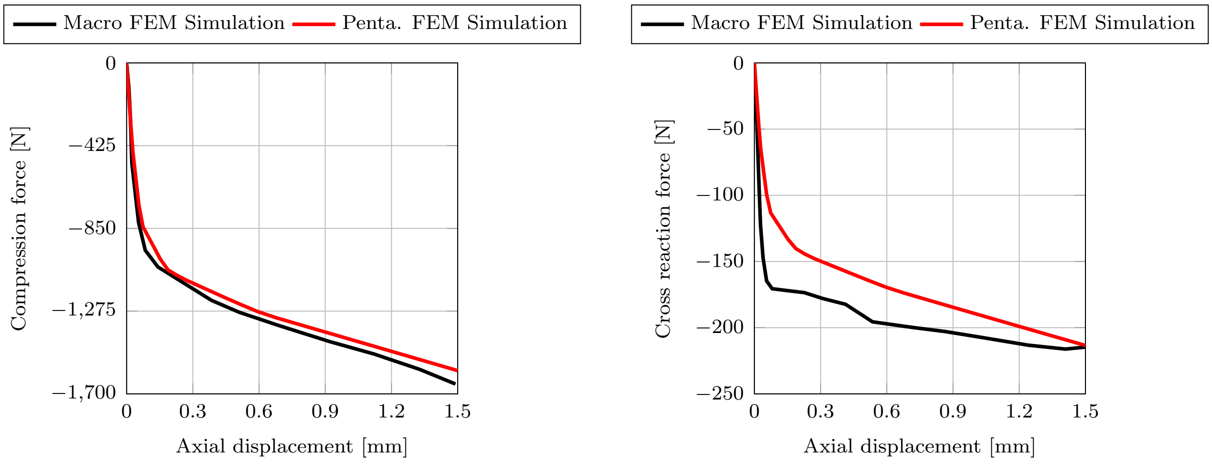

c.1)

c.2)

Figure 20: Results for 3 c) subcase: c.1) axial force-displacement curves for constrained compression subcase. c.2) Cross reaction forces for axial constrained compression subcase.

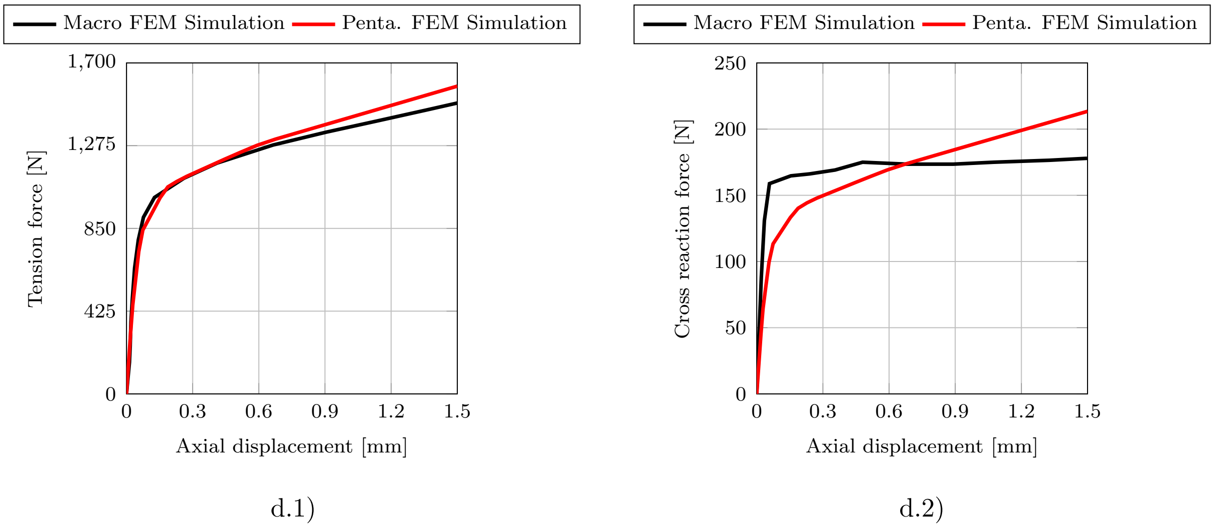

d.1) d.2)

Figure 21: Results for subcase 3 d): d.1) Axial for displacement curve for tension load subcase. d.2) Cross reaction forces for axial constrained tension subcase.

Based on the results obtained, it is determined that the correlation is robust (using the same calibration curves for bars with identical dimensions and slenderness as in the previous case, and a proportionally scaled curve for the longest bar). These types of simulations validate the robustness of the methodology under different loading conditions and boundary scenarios, with the introduction of the correction factor ensuring accurate reproduction of the boundary conditions. On the other hand, the GAM cell in the non-auxetic configuration is analyzed. Although the cells may appear nearly identical, the change in the vertically connected bars makes the cell entirely different, and the stress state of the bars changes completely under the same loading condition. For this reason, this specific cell requires its own calibration curves. Specifically, the bar whose stress state has changed is the medium-length bar, which has shifted from tension to compression. This has led to a significant increase in its calibration curve, while the other bars remain under the same stress states as in the auxetic GAM cell. Therefore, the short bar retains the previous calibration curve, and the curve for the longest bar is obtained by proportionally scaling the original calibration curve for that bar, as shown in the following figure:

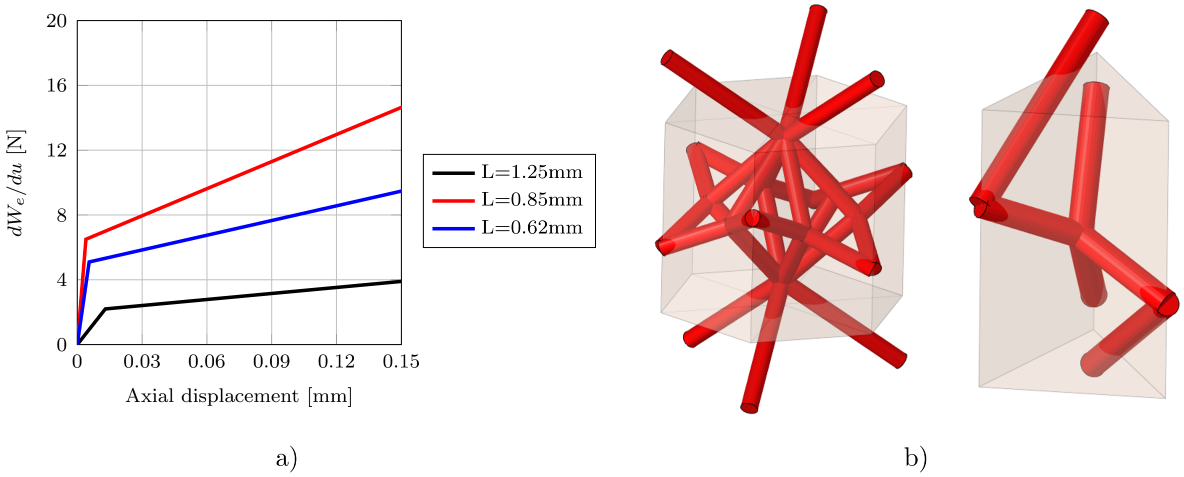

a) b)

Figure 22: a) calibration curves for GAM non auxetic cell, with a radius if $R = 0.07mm$, elastic plastic material model and contact between bars. b) Bars contained inside pentahedral element for GAM non auxetic cell.

Additionally, material parameters for GAM non auxetic configuration for pentahedral model are exposed in Table 2. Taking all this into account, subcases e) and f), corresponding to free axial compression and tension for the non-auxetic GAM cell, are analyzed. Additionally, subcases g) and h), corresponding to constrained axial compression and tension for the same cell, are also examined. Unlike the previous case, the behavior of this cell, as well as its non-auxetic nature, made it unnecessary to introduce any correction factor to accurately reproduce the lateral boundary conditions. The results are presented in the following figures:

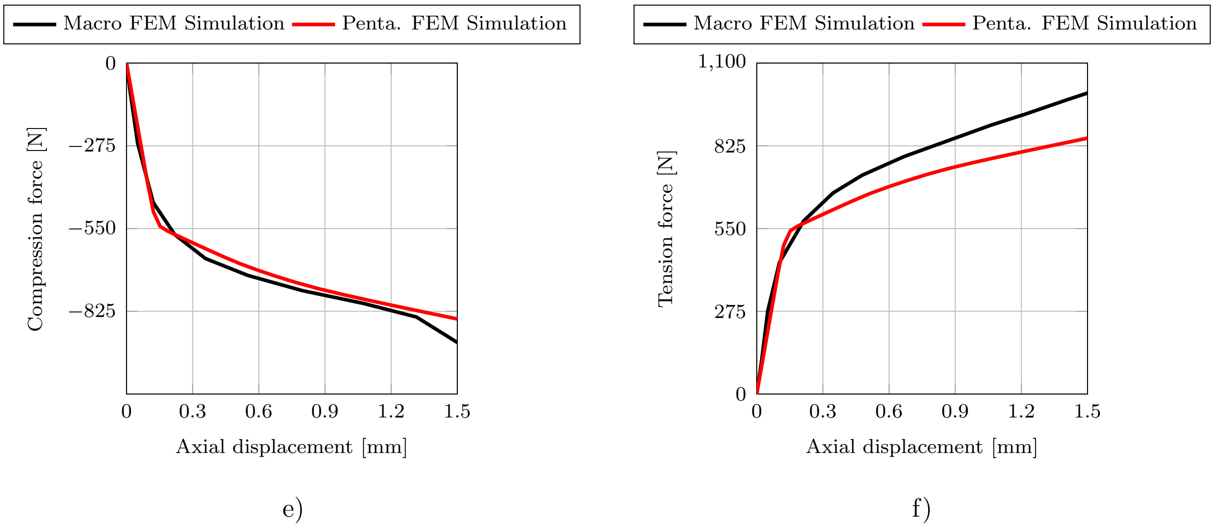

Figure 23: Results for 3 e) and 3 f) subcases: e) Axial force-displacement curve for compression load subcase. f) Axial force-displacement curve for axial load subcase.

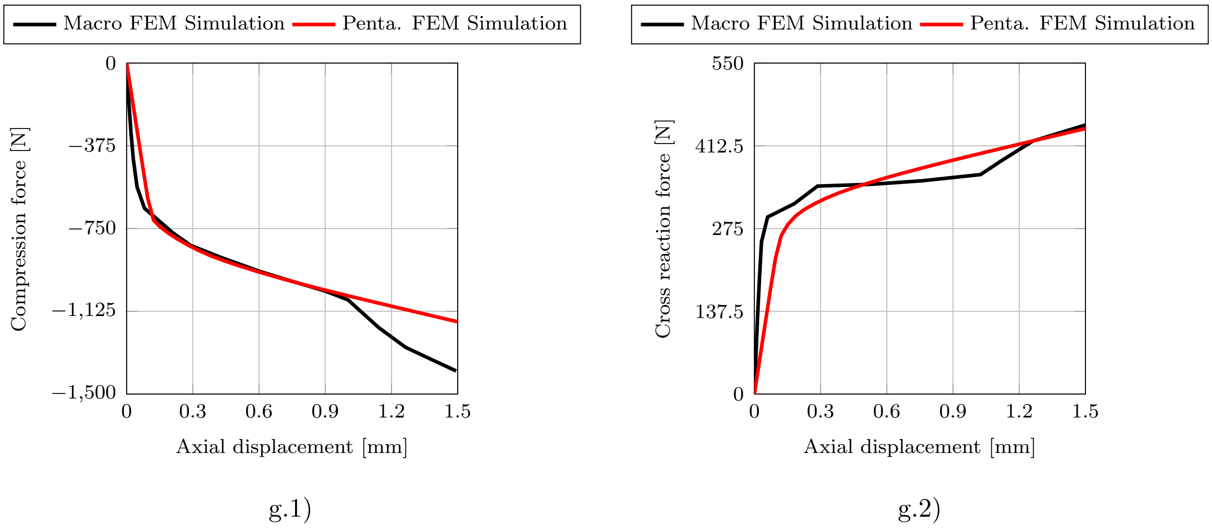

Figure 24: Results for 3 g) subcase: g.1) axial force-displacement curve for constrained compression subcase. g.2) cross reaction forces for constrained compression subcase.

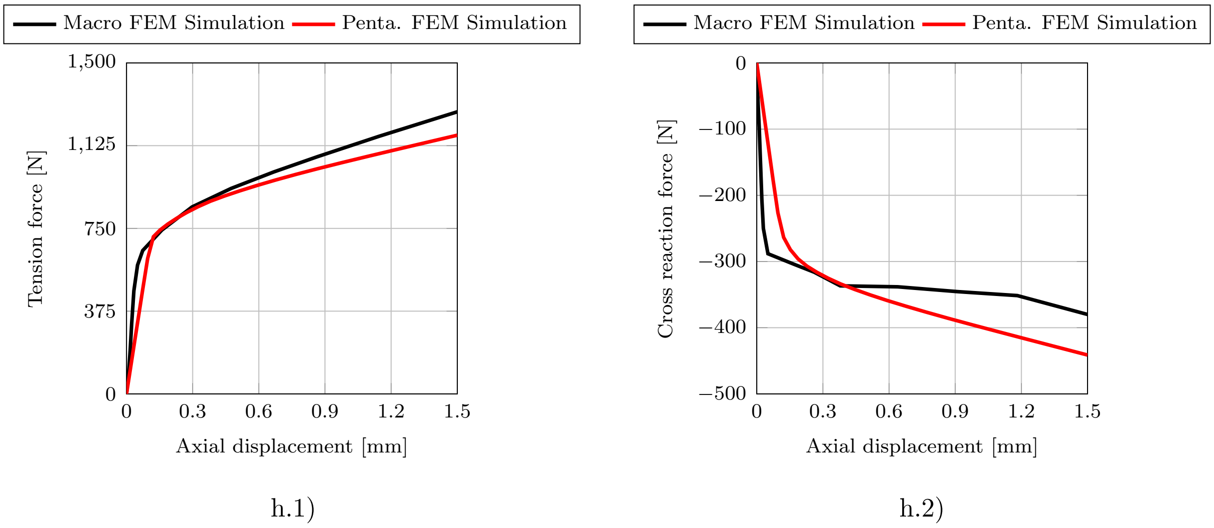

h.1)

h.2)

Figure 25: Results for 3 h) subcase: h.1) axial force-displacement curve for constrained tension subcase. g.2) cross reaction forces for constrained tension subcase.

Stress field for the free GAM subcases in the detailed model are shown too:

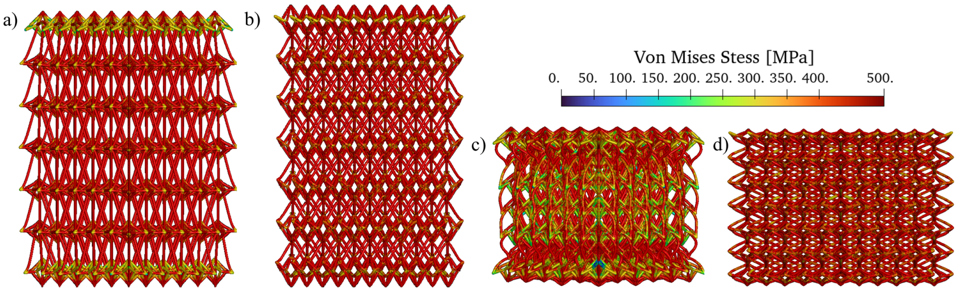

Figure 26: a) Free tension subcase for GAM auxetic structure. b) Free tension subcase for GAM non auxetic structure. c) Free compression subcase for GAM auxetic structure. d) Free compression subcase for GAM non auxetic structure

Based on the results obtained, several relevant conclusions can be drawn from this case:

- The correlation is robust. For each case, the calibration curves used can be extended to five different curves with simultaneous and accurate fitting. The methodology proves to be robust and adaptable to different volumes, loading cases, and boundary conditions, adjusting the calibrations to the corresponding cell parameters, material models, and nonlinear effects such as bar contact interactions.

- The cross boundary conditions for the pentahedral model may not fully reproduce the effect of constraining the boundary vertices of the detailed model. Therefore, a correction factor is introduced to compensate for this and accurately replicate the boundary condition.

- Changing the configuration while maintaining the same cell parameters (from auxetic to non-auxetic configuration) completely alters the nature and behavior of the cell, effectively resulting in a new cell.

- A quantitative analysis of the results shows that the auxetic configuration exhibits greater strength under identical loading conditions compared to the non-auxetic configuration. It is thus concluded that auxeticity is beneficial for the structural performance.

3.4. Case four: complex nonlinear cases. Indentations.

A more complex case is developed now, representing an evolution of the previous cases. Building upon the correlation established in the previous analysis for the GAM cell in the auxetic configuration (and assuming the same cell parameters, bar radius, material model, and contact interactions) a strongly nonlinear simulation is proposed, focusing on an indentation process applied to the metamaterial structure.

To this end, a larger domain of 10x10x7 cells is considered, and a spherical indenter with a radius of 4 mm is used. The penetration depth to be studied is 1.5mm inside the structure. In the detailed model, contact interfaces are included both between the bars themselves and between the indenter and the bar structure. For simplicity, as in previous cases, only one-quarter of the detailed model is simulated, applying equivalent boundary conditions to reduce computational cost as much as possible.

In addition, an equivalent continuum model using pentahedral elements is developed, in which several modeling assumptions are made for this scenario. In this case, the spherical indenter is not explicitly modeled. Instead, its imprint on the structure is introduced into the pentahedral model through progressively applied imposed displacements that simulate the sphere's penetration into the structure. Additionally, any sliding between the indenter and the structure is neglected, and a perfect tied contact is assumed.

Under these considerations, the full pentahedral element model for the indentation case is developed, and the results are presented below:

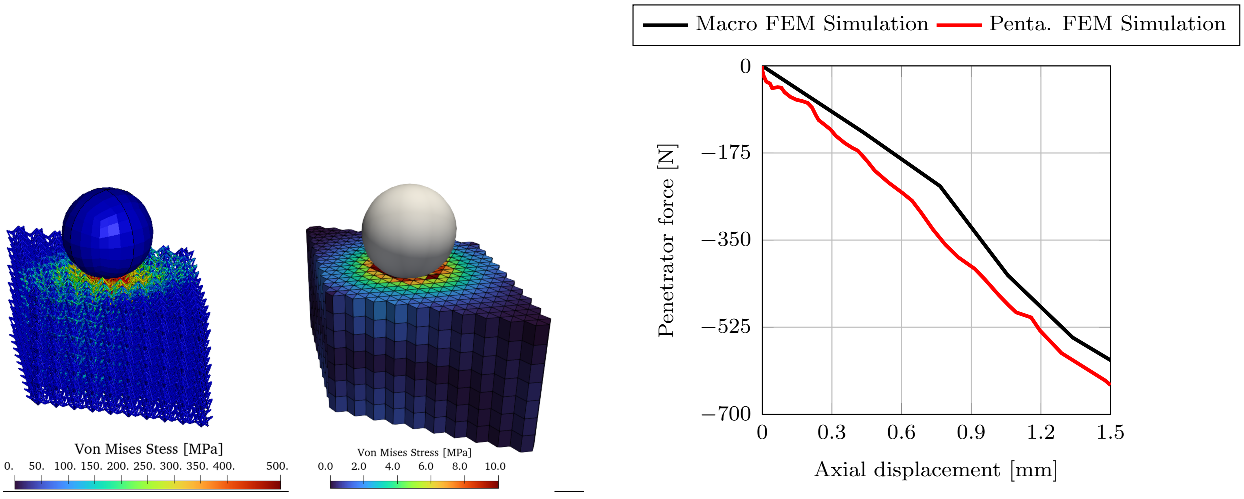

a) b)

Figure 27: a) Stress field for both detailed and pentahedral FEM models for indentation case. b) Penetrator force for both detailed and pentahedral FEM models for intentation case.

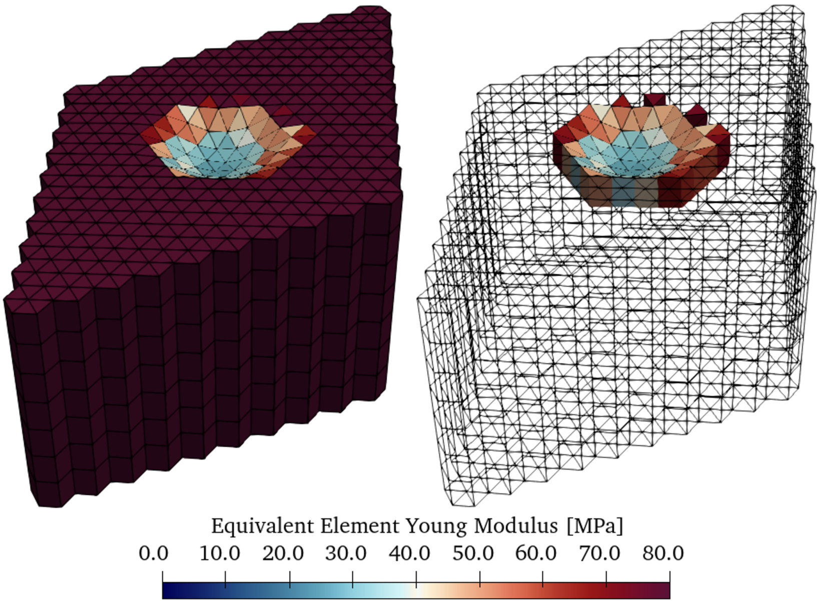

Figure 28: Equivalent Young Modulus reduction at penetration region for pentahedral simulation.

As shown in the results, the force recorded in the indenter (after being multiplied by four, since only a quarter of the detailed model was simulated) correlates accurately with the continuum model (which was entirely simulated), demonstrating that the methodology is robust for this case. As a limitation, the continuum model only allows the simulation of small penetration depths, since the stiffness loss in the elements within the penetration region is significant, leading to local failure of the structure in those elements. On the other hand, it is important to note the differences in the magnitude of the recorded stresses, with a similar effect observed in previous studies. However, the stress distributions are qualitatively similar, with higher stresses near the indentation area, spreading in a spherical manner throughout the continuum structure.

3.5. Case five: different auxetic cell structure cases.

Finally, a case is proposed in which a different cell is analyzed. In this instance, a well-known and widely studied cell is used for the characterization of auxetic behavior, in its 3D configuration. This cell is replicated using the previously described pattern structure, and both lattice and equivalent continuum models based on this pattern are developed. Specifically, a detailed model composed of 3x3x7 patterns is built, employing an elastoplastic material model with isotropic hardening. Additionally, contact interactions between bars are included, and a quarter of the model is simulated using equivalent boundary conditions.

In the continuum model, the same pattern structure is replicated using penta elements, allowing for the complete model to be developed and analyzed. The material parameters used for this type of cell in the continuum model are listed in Table 2.

Four subcases are proposed: a) free axial compression; b) free axial tension; c) axial compression with constrained cross displacements; and d) axial tension with constrained cross displacements. This allows for a quantitative analysis of the effect of auxetic behavior on the structure, while also enabling direct comparison with other cell topologies, such as the GAM cell. As shown in Figure (8), most of the bars that form this cell are located along the edges of the penta element. This directly influences the boundary condition applied, as the restriction of the perimeter nodes becomes even less accurate in this case, given that in the detailed model the entire bar is constrained as a continuous element at the boundary. To address this issue, a new correlation factor is introduced to help mitigate the difficulty. In this case, correction factor implemented is $\alpha = 6.5$, which is quite higher than the one used in GAM auxetic case, showing that the constrain for the penta model is less accurate in this case.

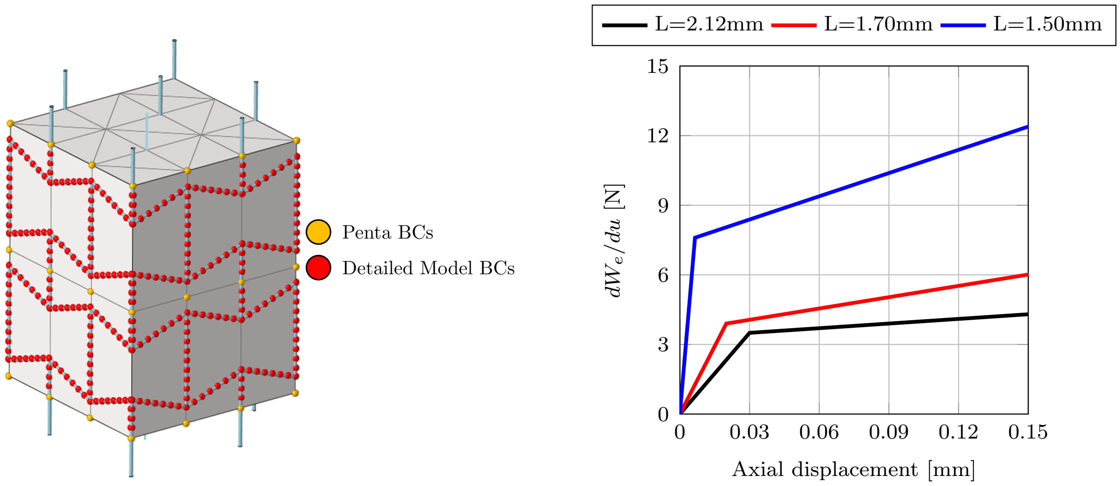

a)

b)

Figure 29: a) Contour boundary condition for both deailed and penta model for GAM auxetic structure. b) Elastic energy correlation curves for GAM auxetic cell, considering $R = 0.07$ mm, nominal cell height, elastic plastic material and contact between bars.

Additionally, new calibration curves are developed for this newly proposed cell topology. Taking these considerations into account, the subcases are analyzed and the results are presented below:

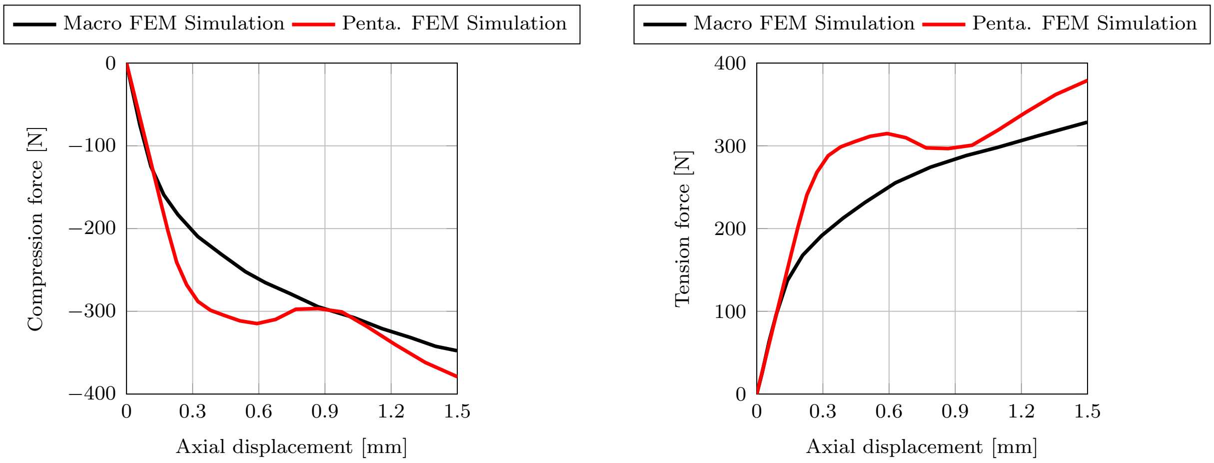

a.1)

a.2)

Figure 30: Results for 5 a) and 5 b) subcases: a) Axial force-displacement curve for free compresion subcase for Cubic cell. b) Axial force-displacement curve for free tension subcase for Cubic cell.

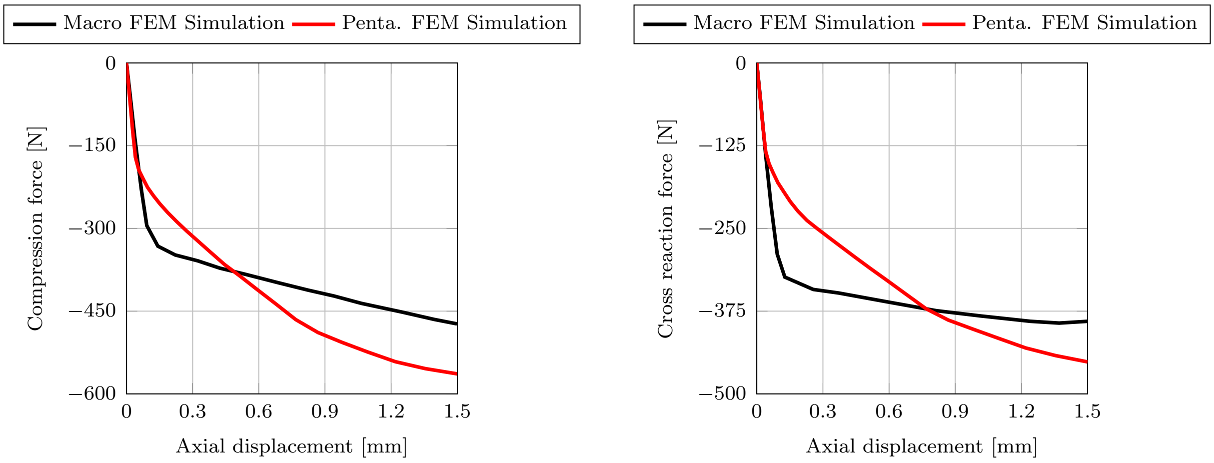

c.1) c.2)

Figure 31: Results for 5 c) subcase: c.1) axial force-displacement curve for constrained compression load subcase. c.2) cross forces along axial distance for constrained compression load subcase.

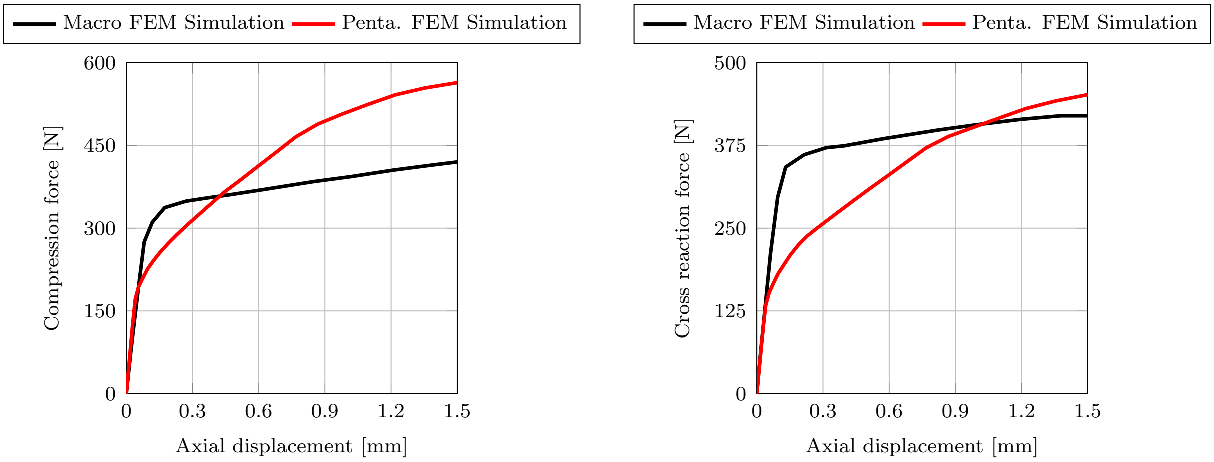

d.1) d.2)

Figure 32: Results for 5 d) subcase: d.1) axial force-displacement curve for constrained tension load subcase. d.2) cross forces along axial distance for constrained tension load subcase.

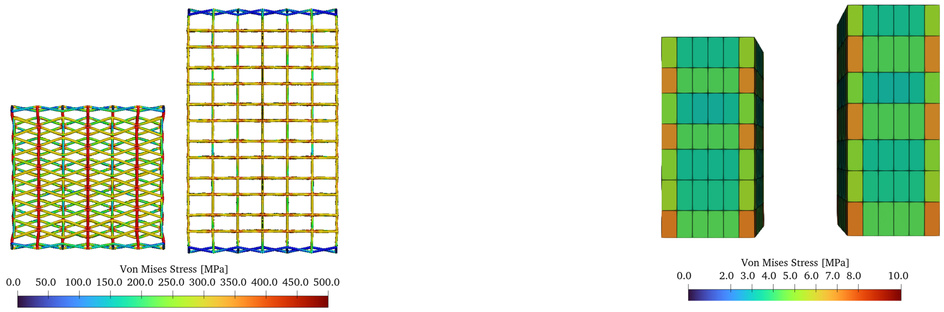

a) b)

Figure 33: a) Stress field for both free compression and tension load subcases for Cubic cell. Detailed model. b) Stress field for both free compression and tension load subcases for Cubic cell. Penta model.

Based on the results obtained, several conclusions can be drawn from this case:

- The correlation is satisfactory. Although it is not as precise as in previous cases, it provides a reasonably accurate approximation of the response of the analogous metamaterial structure, with significantly lower computational cost.
- The boundary condition is less accurate than in the case of the GAM cell. In this scenario, all degrees of freedom of the bar nodes located on the boundary edges are fully constrained for the detailed model, whereas in the continuum model, this condition only applies to the contour nodes of the pentahedral structure. This substantially reduces the accuracy of the results and requires a higher correction factor to better capture the auxetic effect.
- Quantitatively, it is observed that the strength of this structure (despite having a similar material volume to previous structures) is considerably lower. Therefore, the GAM cell remains the auxetic cell with the greatest potential for structural applications.
- The stress state in the continuum structure is averaged across the element, and no local failure is detected in the bars contained within it.

3.5.1. Computational cost analysis.

Finally, a detailed analysis of the computational cost of all the simulations is conducted, making a comparison to those using the proposed methodology. Firstly, it is important to note that the detailed simulations were run on a workstation specifically dedicated to computation, which allows for parallel processing to accelerate computational processes. This workstation has 20 cores and 32 GB of RAM. In contrast, the simulations using the pentahedron analogy were carried out on a standard office computer without parallel processing, with 16 cores (with only one assigned to computing) and 16 GB of RAM. Two bar charts illustrating the potential advantages of the methodology are shown below.

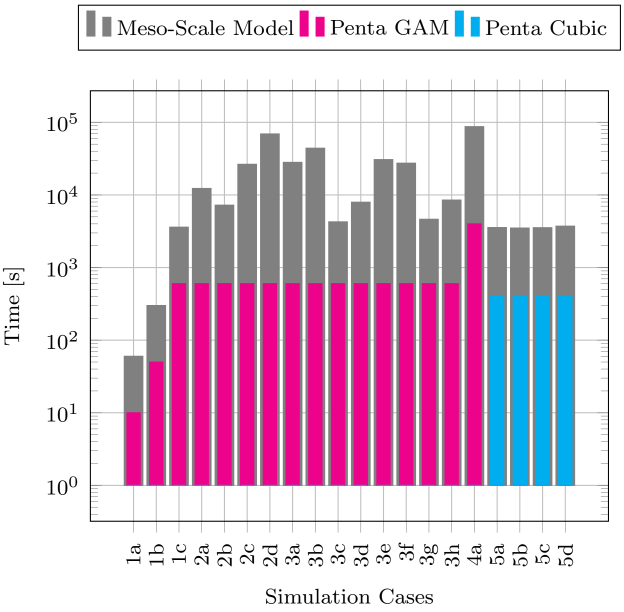

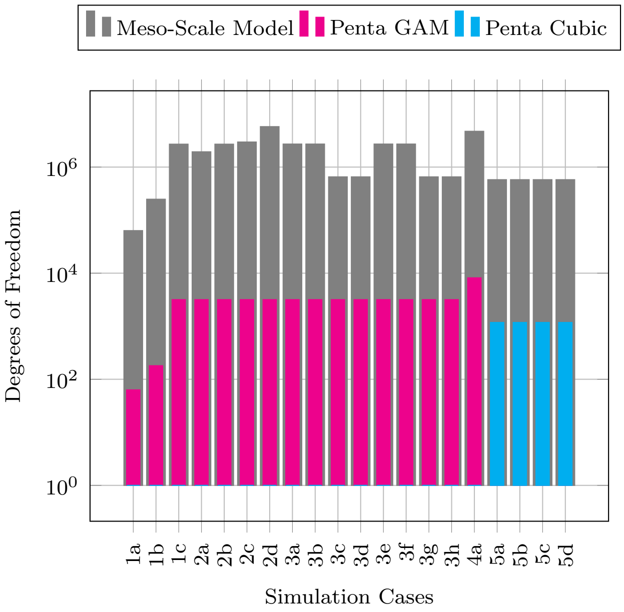

As shown in the figures, even when launched on a machine with lower performance and without parallel computing, considerable gains in computation time are achieved in all the analysed sub-cases. The most evident case is 4a), which shows a reduction of two orders of magnitude in DOFs, which results in a reduction in computation calculation time from one day to one hour. These graphs demonstrate the significant potential of the developed methodology for accurately and rapidly analysing mesoscale models, with the possibility of extending it to macroscale structures of complex geometry at an affordable computational cost.

3.6. Case 6: experimental correlation.

To finalize the validation of the methodology, a new cell for correlation is proposed. In this case, the cell studied in reference [2] is used. In that work, Andrade, Zhu, Miranda, and Rodrigues propose a FEM simulation model in which they simulate the tensile behavior of a two-dimensional auxetic cell, and also develop a FEM model to simulate the compressive behavior of a three-dimensional auxetic cell. Additionally, they compare the obtained results with the experimental manufacturing of the simulated cells, conducting both tensile and compressive tests, thereby providing a real comparison between the simulated and the tested models.

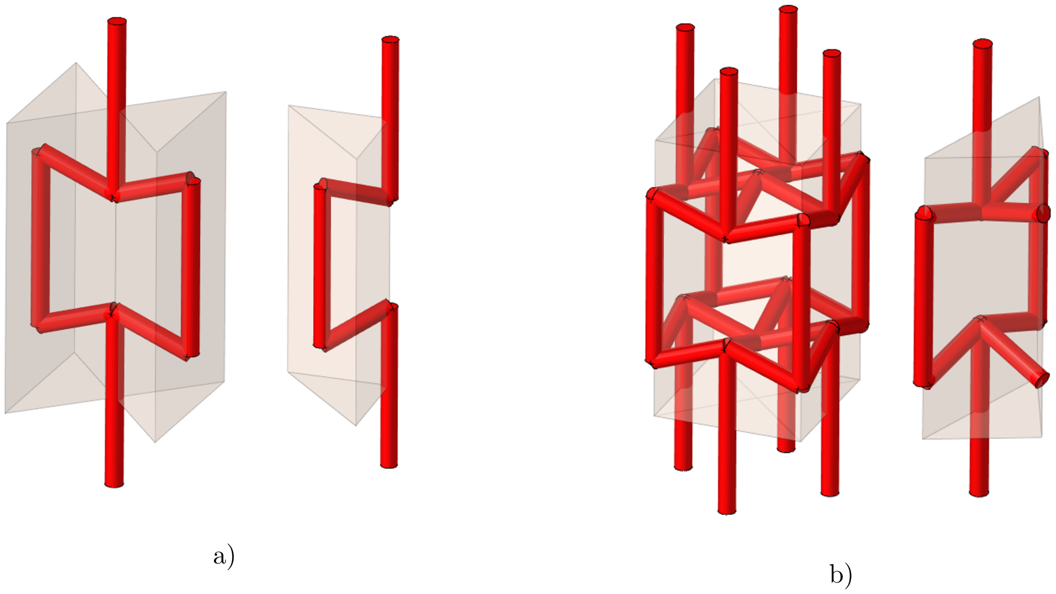
a)

b)

Figure 34: a) Bars inside Penta for 2D auxetic cell. b) Bars inside Penta for 3D auxetic cell.

In this study, the FEM and experimental results obtained in the work done by Andrade et al are used to validate the simulation methodology employing penta elements. For this purpose, equivalent meshes composed of penta elements are established, using the cell dimensions reported in the referenced work. The material parameters used in the penta elements are presented in Table 2. Figure 34 shows the bar structures contained within each penta element, as well as the proposed pentahedral structures for each cell.

Once both subcases have been presented, the calibration of the curves and the analysis of the obtained results are carried out. In each subcase, a calibration has been performed for the experimental data, capturing the existing nonlinearity. Additionally, the calibration is adjusted for both the ideal and as-built simulation models.

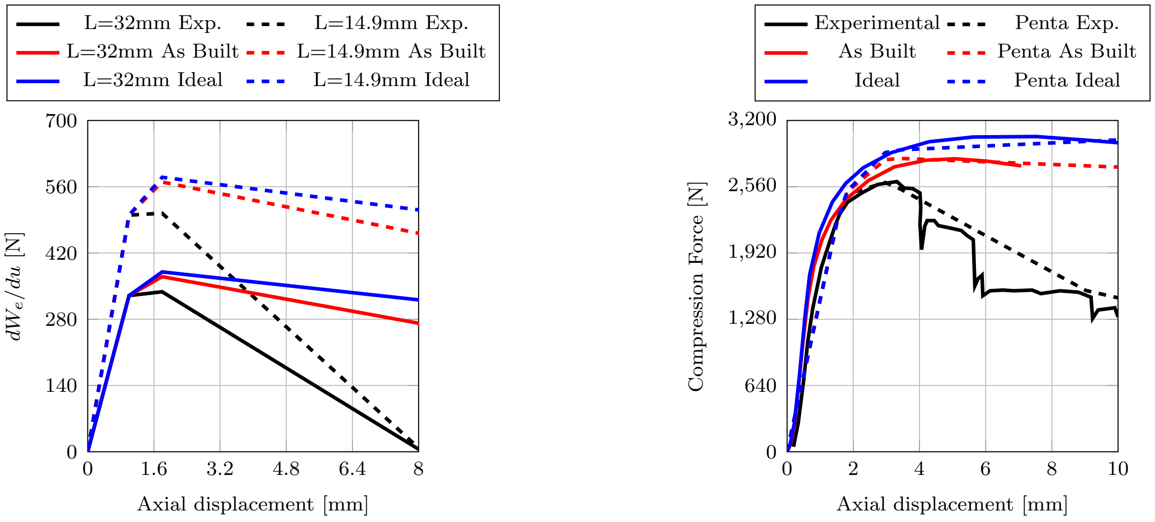

a.1)

a.2)

Figure 35: Results for 6 a) 3D cell subcase subcase: a.1) Calibration curves for both simulations and experimental tests. a.2) Axial compression force-displacement curves correlation for each test.

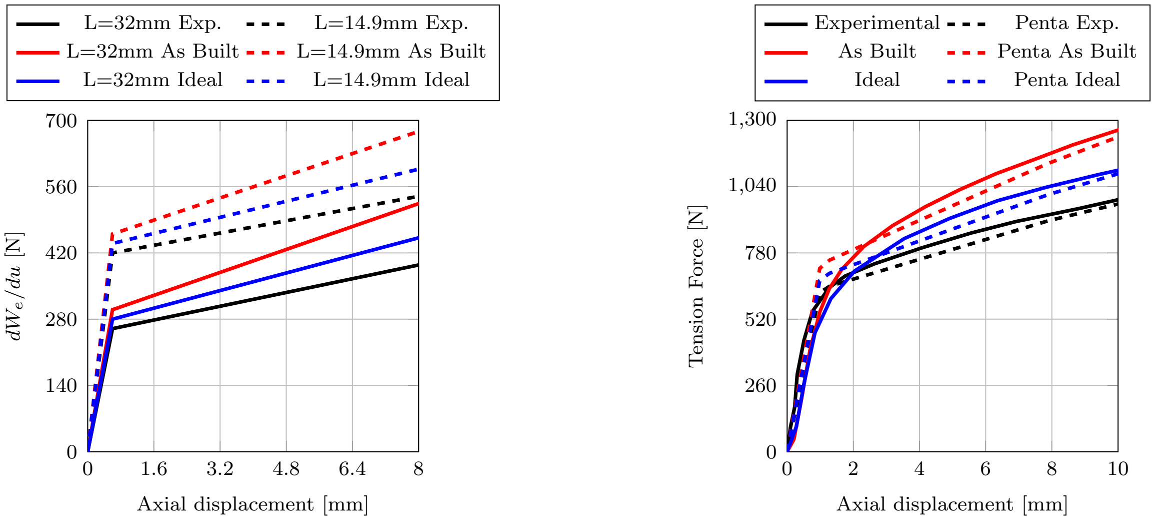

b.1)

b.2)

Figure 36: Results for 6 b) 2D cell subcase: b.1) Calibration curves for both simulations and experimental tests. b.2) Axial compression force-displacement curves correlation for each test.

In view of the obtained results, the robustness of the correlation is confirmed again. In this case, the correlation was performed using a real tested model, which exhibited nonlinear behavior under compression that was successfully reproduced by the continuum model, while the FEM models were unable to do so. It is important to highlight that the geometric changes in the cells, along with the variation in the stress state of the bars, induce a different mechanical nature in each cell; therefore, specific correlations have been developed for each typology. Furthermore, with proper adjustment of the calibration curves, the behavior observed in the FEM models can also be accurately captured.

4. Conclusions

The capabilities of the wTCM element are validated with numerical and experimental data, showing a reduction of the computational cost in ore than 2 orders of magnitude compared with the explicit FEM of the lattices. Also, the use of this proposed element links two traditional problems of structural metamaterials. On one hand, the generative design of metamaterials based on pentahedral elements allows us to create complex cell geometries to be adapted to irregular volumes and patterns. This innovative approach for the lattice generation creates an approach to design transition structures with the use of concepts such as Voronoi tessellations, which define the pentahedral elements that form the resulting lattices. Those can appear between different sizes or arrangements of the same cell type, or even between entirely different cell types.

Furthermore, the proposed design methodology enables the generation of metamaterial structures that are heterogeneous at the macroscale, tailoring the requirements of a component to the most suitable lattice cell configuration in each region. This approach also allows the development of complex 3D geometries that are extremely difficult to achieve using conventional design tools, which become ineffective beyond a certain number of struts in lattice structures.

In parallel with the design approach, a novel and efficient computational methodology has been proposed to analyze metamaterial structures through the wTCM element. The equivalence established between auxetic strut-based structures and pentahedral elements—achieved through the study of strut arrangement within the pentahedral unit—allows for a significant reduction in computational cost, improving performance by several orders of magnitude compared to traditional solid models.

Additionally, the calibration of these simulation models accounts for small nonlinear effects such as strut buckling and the resulting loss of stiffness, as demonstrated through the correlation developed against experimental testing on this work.

In the cases where a lateral restriction is imposed into the wTCM a small lack of accuracy is shown, and it is reduced by a lateral factor in those cases. Also, the precision of the wTCM is influenced by the amount of bars internal to the element, and can have a lower precision when a significant amount of bars go though the edges of the wedge and are shared between several elements.

Annex

Algorithm 3 Pentahedral FEM Algorithm

```
Require: Load case configuration (mesh, boundary conditions, imposed displacements,case type, cell type, material parameters).
Ensure: FEM resolution at each displacement step including equivalence to metamaterial model.
Define Residual force value to convergence
for $u = u_0$ to $u = u_{end}$ do
    while $|\mathbf{f_{glob_i}} - \mathbf{f_{glob_{i-1}}}| < \mathbf{f_{res}}$ do
        Update Young Modulus for each element
        Calculate Local stiffness matrix, $\mathbf{K_{loc}}$, updating material tensor.
        Calculate Global stiffness matrix, $\mathbf{K_{glob}}$, assembly.
        Calculate Reduced flobal stiffness matrix, $\mathbf{K_{red}}$.
        Calculate Equivalent forces vector, $\mathbf{f_{eq}}$.
        Calculate Free nodal displacements, $\mathbf{U_{red}}$.
        Calculate Global nodal displacements, $\mathbf{U_{glob}}$.
        Calculate Global nodal forces, $\mathbf{f_{glob}}$.
        Calculate Global stress tensor for each element, $\boldsymbol{\sigma_{elem}}$.
        Calculate Global strain tensor, $\boldsymbol{\varepsilon_{elem}}$.
        for $elem_j$ in all elements do
            Calculate Element strain energy (without E), $U_{penta,elem}$,as Eq. (6)
            for $bar_k$ in all element inner bars do
                Calculate axial bar strain, $\varepsilon_{bar}$, as in Eq. (1)
                Calculate axial bar displacement, $u_{bar}$, as in Eq. (2)
                Get bar external work gradient, $dW_e/du$, obtained from curves interpolation
            end for
            Calculate element strain energy from bars, $U_{bar,elem}$, as in Eq. (3)
        end for
        if $|\mathbf{f_{glob_i}} - \mathbf{f_{glob_{i-1}}}| < \mathbf{f_{res}}$ then
            Convergence is achieved: Move to next load step.
        else
            Update Element Young Modulus, $E_{updated,elem}$, as in Eq. (7)
            Update i-1 global force vector, $f_{i-1}$.
        end if
    end while
end for
```

References

[1] A. Alderson and K.E. Evans. Modelling of the mechanical properties of polymeric auxetic foams. *Journal of Materials Science*, 37:939–948, 2002.

[2] David Andrade, Carlos Zhu, Hélio Miranda, and Dulce Rodrigues. Metallic 2d and 3d re-entrant honeycomb auxetics produced by waam. *The International Journal of Advanced Manufacturing Technology*, 135:5733–5745, 2024.

[3] S. Babaee, J. Shim, J.C. Weaver, E.R. Chen, N. Patel, and K. Bertoldi. 3d soft metamaterials with negative poisson's ratio. *Advanced Materials*, 25(36):5044–5049, 2013.

[4] K. J. Bathe. *Finite Element Procedures*. Prentice Hall, Englewood Cliffs, NJ, 1996.

[5] Ismael Ben-Yelun, Guillermo Carano, Francisco Millán, Miguel Gomez, Francisco Leal, and Luis Saucedo Mora. The gam (general auxetic metamaterial): A tuneable internal structural configuration to change the auxetic response with the same unit cell boundary geometry. *SSRN Electronic Journal*, 01 2022.

[6] Katia Bertoldi, Vincenzo Vitelli, Johan Christensen, and Martin van Hecke. Flexible mechanical metamaterials. *Nature Reviews Materials*, 2:17066, 2017.

[7] A. Clausen, F. Wang, J.S. Jensen, O. Sigmund, and J.A. Lewis. Topology optimized architectures with programmable poisson's ratio over large deformations. *Advanced Materials*, 27(37):5523–5527, 2015.

[8] Hooman Danesh, Daniele Di Lorenzo, Francisco Chinesta, Stefanie Reese, and Tim Brepols. Fft-based surrogate modeling of auxetic metamaterials with real-time prediction of effective elastic properties and swift inverse design, 2024.

[9] Ioannis Dassios, Georgios Tzounas, Federico Milano, and Andrey Jivkov. A discrete model for force-based elasticity and plasticity. *Journal of Computational and Applied Mathematics*, 444:115796, 2024.

[10] J.N. Grima and K.E. Evans. Auxetic behavior from rotating squares. *Journal of Materials Science Letters*, 19:1563–1565, 2000.

[11] H.M.A. Kolken and A.A. Zadpoor. Auxetic mechanical metamaterials. *RSC Advances*, 7:5111–5129, 2017.

[12] R. Lakes. Foam structures with a negative poisson's ratio. *Science*, 235(4792):1038–1040, 1987.

[13] Z. Liu, X. Zhang, Y. Mao, Y.Y. Zhu, Z. Yang, C.T. Chan, and P. Sheng. Locally resonant sonic materials. *Science*, 289(5485):1734–1736, 2000.

[14] Livermore Software Technology (LST). *LS-DYNA Theory Manual.* Livermore, CA, 2022. Section 4.8, page 25.

[15] Steve Maas, Dave Rawlins, Jeffrey Weiss, and Gerard Ateshian. Febio theory manual, version 2.7, section 4.1.2, 2018. accessed on 2025-04-01.

[16] M.J. Mirzaali, M. Moghadasi, and A.A. Zadpoor. Mechanical metamaterials with functionally graded auxeticity. *Advanced Materials*, 32(25):1907822, 2020.

[17] J.B. Pendry, A.J. Holden, D.J. Robbins, and W.J. Stewart. Magnetism from conductors and enhanced nonlinear phenomena. *IEEE Transactions on Microwave Theory and Techniques*, 47(11):2075–2084, 1999.

[18] D. Prall and R.S. Lakes. Properties of a chiral honeycomb with a poisson's ratio of -1. *International Journal of Mechanical Sciences*, 39(3):305–314, 1997.

[19] X. Ren, R. Das, P. Tran, T.D. Ngo, and Y.M. Xie. Auxetic metamaterials and structures: a review. *Smart Materials and Structures*, 27(2):023001, 2018.

[20] Xin Ren, Raj Das, Phuong Tran, Tuan Duc Ngo, and Yi Min Xie. Auxetic metamaterials and structures: a review. *Smart Materials and Structures*, 27(2):023001, jan 2018.

[21] Luis Saucedo Mora, Guillermo Gómez Carano, Miguel Ángel Sanz Gómez, and Francisco Javier Montáns Leal.

[22] J. Ulloa, M.P. Ariza, J.E. Andrade, and M. Ortiz. Homogenized models of mechanical metamaterials. *Computer Methods in Applied Mechanics and Engineering*, 433:117454, 2025.

[23] Z. Wang, Z. Zhang, Q. Shi, T. He, and C. Lee. Design and application of auxetic structures in flexible devices: a review. *Advanced Functional Materials*, 30(3):1903125, 2020.

[24] W. Yang, Z.M. Li, W. Shi, B.H. Xie, and M.B. Yang. Review on auxetic materials. *Journal of Materials Science*, 39(10):3269–3279, 2004.

[25] H. Yasuda and J. Yang. Reentrant origami-based metamaterials with negative poisson's ratio and bistability. *Physical Review Letters*, 114(18):185502, 2015.

[26] S. Yuan, F. Shen, C.K. Chua, and K. Zhou. 3d printed auxetic structures with tunable mechanical properties. *Materials & Design*, 182:108010, 2019.